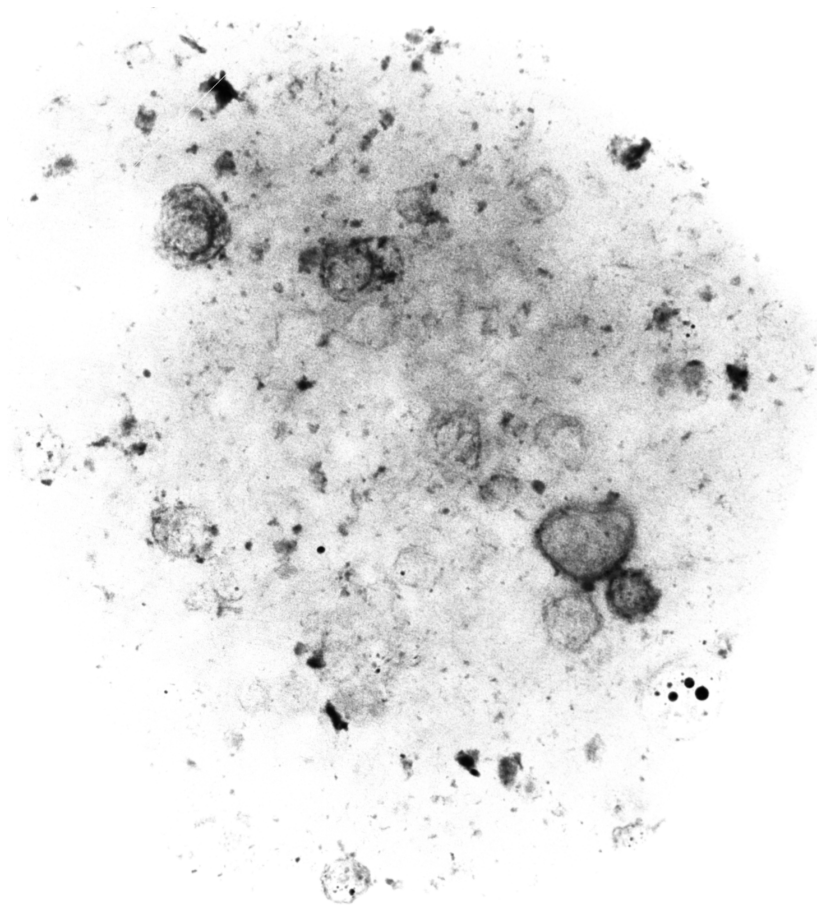


Bachelor Thesis

X-ray and Neutron Tomography of the Allende Meteorite

Røntgen- og Neutrontomografi på Allende-meteoritten



Sandra Steen Duchnik, Mika Lanzky, and Louise Steffensen Schmidt

Supervisor: Kim Lefmann

Niels Bohr Institutet
Københavns Universitet

1st of June, 2012

X-ray and neutron tomography of the Allende-meteorite

This bachelor thesis is a collaborative work between all the (co)writers listed below, therefore the individual contributions are *not* identified. All text, dataprocessing, imaging, and calculations are submitted for review as a joint venture and are to be evaluated as such.

Denne bachelor rapport er et fælles arbejde mellem alle nedenstående (med)forfattere, derfor er de individuelle bidrag *ikke* identificeret. Al tekst, databehandling, afbildninger og udregninger afleveres til gennemgang som et samarbejde og skal evalueres således.

Sandra Steen Duchnik (0211861444)
ghk339@alumni.ku.dk

Mika Lanzky (1208892580)
mdw675@alumni.ku.dk

Louise Steffensen Schmidt (1012881580)
kxv358@alumni.ku.dk

Abstract

Meteorites constitute a scarce and significant resource in the natural sciences, some of which only direct information about the earliest stages of the Solar System.

The traditional way of investigation the interior of a stone is thin sections, a technique that does not reveal everything about the sample, nor does it preserve the original information. Now meteorites can be investigated with non-destructive 3D imaging techniques without damaging the rare samples, thus giving an inference of both composition and structure.

We used the complementary features of X-ray and neutron tomography to further investigate an inclusion in a piece of the CV-meteorite Allende that had previously been identified with neutron tomography at PSI in 2005. We did this by performing a X-ray experiment on the piece at Novo Nordisk as well as repeat the neutron experiment at PSI at a higher resolution

Like others, we found that the morphology of a meteorite can be distinguished in X-ray images due to varying attenuation coefficients, and that it could be distinguished in high-resolution neutron images as well. Chondrules, CAIs, matrix and metal-mineral grain inclusions have all been identified in both our X-ray and high-resolution neutron images.

We found that the inclusion has high attenuation in *both* X-ray and neutron images, appearing as an oval shape with an indent. Due to its high attenuation in both tomography techniques, a sure determination of its composition as hydrogen is not possible.

The explanation for the inclusion being highly attenuating of both X-rays and neutrons is likely that the rim consists of minerals containing both a X-ray high attenuation metal *and* the neutron high attenuation element hydrogen. This can be gathered by looking at X-ray and neutron images in conjunction.

Higher resolution tomography would make possible spatial differentiation easier to determine, and probing done at lower energies would make the differences between minerals clearer. The latter, however, requires a thinner sample, defeating the purpose of preserving the integrity of the sample.

A weighing of the importance of conserving the stone compared to the possibility of slicing in order to investigate is always an issue. Ideally, non-destructive research technique should always be the first step when investigating a meteorite; as such, tomography is a very useful tool, yielding information about both the chemical and physical composition of the stone. 3D imaging can help determine areas of interest for further research, so damage to the stone is not done in vain.

Resumé

Meteoritter er en sjælden og signifikant informationskilde i naturvidenskaben; nogle af dem giver den eneste direkte information om de tidligste stadier i solsystemets udvikling.

Den traditionelle måde at undersøge indholdet i en sten er ved at skære den i tynde skiver, en teknik som ikke viser alt om prøven, og heller ikke beholder den originale information. Nu kan meteoritter blive undersøgt med ikke-destruktive 3D teknikker uden at beskadige de sjældne prøver, som giver en ide om både stenens sammensætning og struktur.

Vi brugte de komplementære features af røntgen og neutron tomografi til at videre undersøge en inklusion i et stykke af CV-meteoritten Allende, som tidligere var blevet fundet med neutron tomografi hos PSI i 2005. Vi gjorde dette ved at udføre vores eget røntgen eksperiment på stykket hos Novo Nordisk samt gentage neutron eksperimentet hos PSI ved højere opløsning.

Ligesom andre fandt vi, at morfologien af meteoritter kan blive set i røntgen billeder pga. variation i dæmpningskoefficienterne, og de kunne også ses i neutronbillederne i høj opløsning. Kondruler, CAI'er, matrix, og metal-rige mineral inklusioner er alle blevet identificeret i både vores røntgen- og højopløsnings neutronbilleder.

Vi fandt at inklusionen har en høj dæmpning i *både* røntgen- og neutronbillederne, fremstående som en oval form med et indryk. På grund af dens høje dæmpning i begge tomografi-teknikker, kan det ikke med sikkerhed bestemmes om den består af hydrogen.

Forklaringen på, at inklusionen dæmper både røntgenstråler og neutroner meget, kunne være, at kanten består af mineraler der både indeholder et metal, som dæmper røntgenstråler meget, *og* hydrogen, et element som dæmper neutroner meget. Dette blev fundet ved sammenligning af X-ray- og neutronbilleder.

Røntgen tomografi i højere opløsning ville gøre nemmere at bestemme rumlige forskelligheder, og et eksperimentet ved lavere energier ville føre forskelle mellem mineraler mere tydelig. Det sidste ville dog kræve en tyndere prøve, hvilket jo desværre ville beskadige meteoritten.

En vægtning af vigtigheden af at bevare stenen sammenlignet med muligheden for at skære i prøven for at undersøge den er altid et problem. Idealt skulle ikke destruktive forskningsteknikker altid være det første trin når man undersøger en meteorit; derfor er tomografi et meget nyttigt værktøj, som giver information om både den kemiske og fysiske sammensætning af stenen. 3D billeder kan hjælpe med at bestemme interessante områder til videre forskning, så stenen ikke bliver beskåret forgæves.

Foreword and acknowledgements

The foundation for this project was actually laid a year prior to its commencing, when we were following the course 'Experimental Physics' taught by our supervisor to be, Kim Lefmann.

As the final assignment for this course, we worked with Morten Bo Madsen, Kim's old thesis supervisor, on the technique of Mössbauer spectroscopy where we investigated another carbonaceous chondrite, the CM-meteorite Maribo, graciously lent to us by Henning Hack, meteorite curator at the Natural History Museum.

At the end of the course, Kim asked if we were done with meteorites, 'cause if not, he had old data just waiting to be analyzed and even a possible beam time at PSI in Switzerland for a new experiment. Six months later, we started preparations for this project: we once again borrowed a meteorite from Henning Hack, this time the CV chondrite Allende, and the project was quickly expanded to being the combination of X-ray and neutron tomography on the meteorite, with both old and new data.

The work on this project has been both difficult and fun at times. Difficult, because – being primarily geophysics students, the field of solid state physics was more or less completely new to us – we had to learn about tomography and imaging techniques from practically scratch; and fun, because we had to learn these things from scratch.

Many people have helped us with this project, whom we would like to thank.

Robert Feidenhans'l, for introducing us to X-rays, and for always asking if the paper wasn't finished already. Maria Thomsen for her thesis' illustrative figures from which we drew inspiration, and for establishing contact with Mette Poulsen from Novo Nordisk in Hillerød, where we carried out our X-ray experiment. In getting the old neutron data of Allende to work, we got the assistance of Peter Willendrup from DTU. The department of eScience at NBI, especially Brian Vinter and Simon Lund, for helping us getting a working data set that we could actually draw numbers out of. Morten Bo Madsen for getting us started on meteorites a year ago and for helping out in the early stages of this project. For squeezing us in for beamtime at PSI, Switzerland; Christian Grünzweig. David Mannes, PSI, for reconstructing the neutron data. Henning Hack, for being willing to lend us meteorites and teaching us about them. A thank also goes to Martin Micki Pedersen, just because.

And finally, the biggest thanks goes our supervisor, Kim Lefmann, for everything: for help holding the many, many reins of this project, for keeping a level head when we needed it, for introducing us to the world of neutrons, for having an interest in meteorites, and most importantly, for letting us spam him with 'stupid' questions.

1st of June, 2012

Sandra Steen Duchnik, Mika Lanzky, and Louise Steffensen Schmidt

Contents

1	Introduction	1
2	Scientific background	2
2.1	Meteorites	2
2.1.1	Chondritic meteorites	2
2.1.2	Early Solar System Evolution	3
2.1.3	The Allende meteorite	4
2.2	Tomography	5
2.2.1	Attenuation	5
2.2.2	Radon transformation	6
2.2.3	Tomography Geometry	7
2.2.4	X-ray tomography	7
2.2.5	Neutron tomography	9
2.3	Tomography of chondrites	10
3	Method	11
3.1	Our piece of the Allende meteorite	11
3.2	X-ray tomography	11
3.2.1	Beam Attenuation	11
3.2.2	Experimental setup	13
3.2.3	Reconstruction	14
3.3	Neutron tomography	15
3.3.1	Beam attenuation	15
3.3.2	Experimental setup	16
4	Results	17
4.1	X-ray	17
4.2	Neutron data	19
5	Discussion	20
5.1	X-ray tomography	20
5.1.1	Comparison of stone and X-ray	21
5.1.2	Profile plots	21
5.1.3	Histograms	23
5.2	Neutron Tomography	24
5.2.1	Discussion	24
5.2.2	Comparison of stone and neutron	25
5.2.3	Profile plots	25
5.2.4	Histogram	27
5.3	Investigation of the inclusion	28
6	Further research	29
7	Conclusion	30
A	Appendix	34
A.1	Old neutron experiment	34
A.1.1	Experimental setup	34
A.1.2	Results	34
A.1.3	Discussion	34

A.1.4	Profile plot	34
A.1.5	Histogram	36
A.1.6	Old and new data	37
A.2	Comparison of photo and X-ray	38
A.3	X-ray profile plot through droplet	40
A.4	X-ray profile plot through double rims	40
A.5	Comparison of photo and neutron	41

List of Figures

1	3D tomographic image of stone from 2005-data	1
2	The different types of meteorites	3
3	Picture showing CAIs, chondrules, and matrix.	3
4	Radon Transform	5
5	Attenuation of waves	5
6	Field of view and resolution	7
7	Attenuation curves for a few common minerals	8
8	Maxwellian energy distributions for thermal, 300 K, and for cold, 30 K, neutrons . . .	10
9	X-ray on Allende from Friedrich's article	10
10	Pictures of our Allende meteorite sample from different angles.	11
11	Transmission as a function of energy.	13
12	The X-ray experiment setup at Novo	13
13	Schematic drawing of the ray path.	14
14	Transmission as a function of wavelength.	16
15	Schematic drawing of the beam's path.	16
16	Experimental setup in NEUTRA source	17
17	X-ray tomographic image	18
18	X-ray tomographic image	18
19	Histogram for entire 3D tomographic image	19
20	Tiff pictures of the stone	20
21	Normalized histograms for neutron data	20
22	The surface of the stone: X-ray and natural light	21
23	Profile plots through different parts of the meteorite	22
24	Histograms over certain parts of the stone	24
25	The surface of the stone: Neutron and natural light	25
26	Profile plots through different parts of the meteorite	26
27	Histogram: Neutron data	27
28	The shape of the inclusion	28
29	Tomographic images of a core of granite at low and high energies	29
30	Old experimental setup in NEUTRA source	34
31	Tiff pictures of the stone	35
32	Normalized histograms for neutron data	35
33	Profile plots: Old Neutron data	36
34	Histogram: Neutron data	37
35	The stones surface in natural light	38
36	Tomographic image of the stone's surface	39
37	Profile plot through droplets	40
38	Profile plot through double ring	40
39	The stones surface in natural light	41
40	Tomographic image of the stone's surface	42

List of Tables

1	Table of wt%, μ/ρ , and μ	12
2	Table of N, σ_s , $\sigma_{a,th}$, and μ	15
3	Approx μ -values for several of the elements in Allende	24
4	Approx μ -values for several of the components in Allende for neutron	27
5	Approx μ -values for several of the components in Allende for neutron	37

1 Introduction

A planet's placement within a system is crucial if it is to sustain life: the climate needs to be just right, meaning not too cold and not too hot. In order to understand why Earth ended up being, luckily for us, the '3rd rock from the sun', we need to investigate how the Solar System evolved during its early years.

One way to do that is by looking at similar situations: the interdisciplinary field of astrobiology elaborates on the demands of life and guesses to what kind of life could exist, and possibly thrive, in a particular climate. The branch of astrophysics called exoplanetary research is combing through the Milkyway with the aid of the Kepler Satellite in search of Earth-like planets [1] that might fulfill the requirements for having water in liquid form, a pivotal need in order for life to cultivate.

While this provides possible scenarios for the evolution of a solar system, it is not necessarily the exact picture of how *our* solar system formed.

Through hundreds of years of research and experiments, the laws of physics - the laws that govern our existence from the smallest quarks to the biggest galaxies - have been established: we know how things react to each other and how one event influences another, but like in every textbook example we need to apply initial conditions - a $f(0)$ so to speak - in order to model the development of a system, in this case the Solar System, if it is even possible.

Paleontologists study the development of life through the investigation of fossilized remains of both fauna and flora; phylogeneticists use the 'molecular clock' to work their way backwards to a common ancestor of a given group of species by making phylogenetic trees that show the relationship between species and the kingdoms of life themselves; and in order to learn about the Earth's climatic history, geologists study ancient rocks and minerals dating back to 3.8 Ga and 4.4 Ga respectively, possibly providing the earliest evidence of photosynthetic life and a widespread body of water on the surface [2].

Just as these initial conditions are left as only traces, so are the clues to the early stages of the Solar System, of which meteorites can provide insight and understanding. The age of the Solar System, 4.567 Ga [3] as well as the conditions under which the Solar System formed and the composition of the applicable objects are all inferred from meteorites.

In fact, meteorites are the *only* direct link to obtaining knowledge about these early stages, as the building blocks of our own Earth have long ago been remelted and reused in the process called 'the rock cycle', thus obscuring the information they once contained. Meteorites, like terrestrial stones, have different chemical composition and physical objects. By examining how these have been varyingly altered and affected, a hypothesis for the evolution of the Solar System can be proposed.

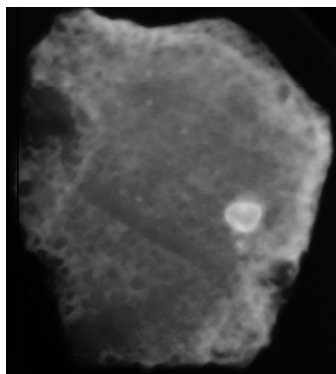


Figure 1: *3D tomographic image of our piece of the Allende meteorite made from data collected at PSI in 2005 by the program Slicer. The round, white inclusion perhaps consists of hydrogen-minerals.*

Meteorites constitute a scarce resource and as such non-destructive research techniques are much preferred. The standard way of investigating their interior is slicing and possibly searing the stones, and the chemical properties are then investigated by mass spectroscopy. Non-destructive methods that

have been used on meteorites include Mössbauer [4] and Raman spectroscopy [5] as well as X-ray [6] and neutron imaging.

Previously, a three-dimensional model of a meteorite or stone could be made by slicing the entire sample into several thin sections, photographing these, and then combining them into a reconstructed 3D-model. Now, this can be done while still preserving the information contained in the sample by using tomography.

X-rays easily go through lighter materials, but their ability to penetrate gets smaller the heavier the element. This makes X-ray tomography show the denser elements because the absorption gives the imaging contrast. Conversely, neutron particles have an especially difficult time going through hydrogen, but can pass easily through most of the heavier elements, thus making neutron tomographic images show primarily hydrogen.

In 2005, a piece of the Allende meteorite was examined with neutron tomography at PSI in Switzerland, showing some interesting inclusions as seen in figure 1.

The goal of this project is therefore two-pronged: by using the complementing techniques of X-ray and neutron tomography we hope to see differentiating inclusions clearer and perhaps in greater numbers, and also show how 3D imaging can be used to investigate a meteorite's morphology and pinpoint regions of interest for further, perhaps more invasive, research.

2 Scientific background

2.1 Meteorites

Meteorites are pieces of extraterrestrial material that have survived the journey through the Earth's atmosphere. The annual influx of meteorites with a mass >10 g is estimated to be between 36 and 116 per 10^6 km² of the Earth's surface [7], giving a total average of about 19-60,000 meteorites per year that lands on the surface. Most of these land in the ocean and only about one percent of the fallen meteorites are found by man. The best place to look for meteorites is large barren places *e.g.* a desert or Antarctica.

They are classified into three main groups (irons, stony-irons, and stones) due to differences in mineralogy and chemical composition. Of the three groups, stony meteorites are the most abundant and are divided into two sub-groups: chondrites (meteorites with primitive and undifferentiated parent bodies) and achondrites (meteorites with a differentiated parent body) [3]. The different types of meteorites and their groups are shown in figure 2. Fall statistics indicate that 86.2% of meteorites on Earth are chondrites, 7.9% achondrites, only 1.1% stony-irons, and 4.8% iron-meteorites [7].

From here on we will only consider chondritic meteorites.

2.1.1 Chondritic meteorites

Chondrites are divided into three classes (Carbonaceous, Ordinary, and Enstatite) and 16 groups based largely on their oxygen isotopic composition and mineralogical properties. All but two groups can be assigned to one of the three classes, as can be seen in figure 2. Each group is then further divided into six petrologic types. Petrologic types 3–6 reflect the level of thermal metamorphism, whereas types 1 and 2 reflect meteorites that are unmetamorphosed, but have experienced different degrees of aqueous alteration. However, many carbonaceous chondrite groups have no known members of types ≥ 4 [8]. Chondrites of type 3 are the most pristine.

The three major components of chondrites are chondrules, matrix, and refractory inclusions, as shown in figure 3.

Chondrules are small, round grains of silicate minerals that formed in minutes to hours in brief, local heating events. Thus chondrules are depleted of elements more volatile than iron, like *e.g.*

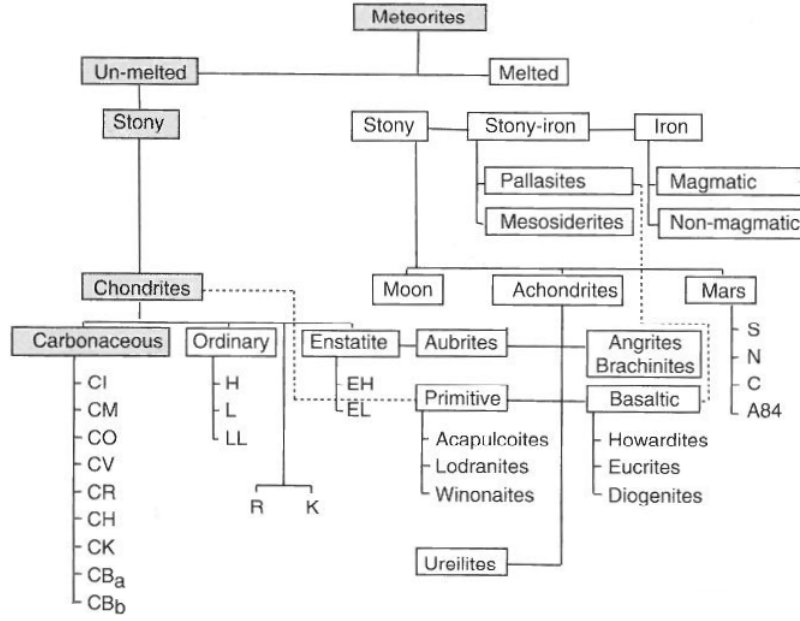


Figure 2: The different meteorite groups and classes. Chondrites are our primary focus in this project; they are divided into 16 groups and 3 classes (Carbonaceous, Ordinary, and Enstatite). The different kinds of carbonaceous chondrites are groups CI-CB_b, ordinary are groups H-LL, enstatite are groups EH and EL, while group R and K does not belong to any of the classes. All meteorites belonging to the same group (e.g. CI) are expected to originate from the same parent body. From [2].

natron. Matrix is the fine-grained material within which the larger components, such as chondrules, are embedded. It mostly consists of silicates. Volatile elements are more abundant in matrix than in any of the other components [3, 9].

There are two types of refractory inclusions: Calcium-Aluminum-rich Inclusions (CAIs) and Amoeboid Olivine Aggregates (AOAs). Both consist of highly refractory minerals *i.e.* minerals composed of elements with very high condensation temperatures, as opposed to volatile elements (which are not necessarily gasses) that condensate at low temperatures. CAIs were formed as condensates or re-melted condensates in a gas of solar composition at the very beginning of the Solar System [3]. Chondrules and CAIs are our only direct clues of the evolution of the protoplanetary disk in the first few Ma.

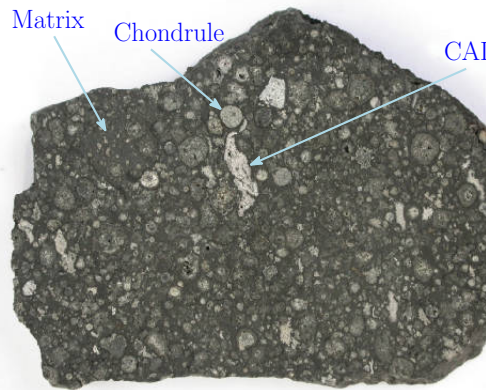


Figure 3: Picture showing CAIs (Calcium Aluminium-rich Inclusions), chondrules, and matrix [10].

2.1.2 Early Solar System Evolution

More than 4.6 billion years ago, inside a large nebula in the Milkyway galaxy, a huge star was generating shock waves. One of these waves made a dense part of the nebula collapse, forming the protosun.

The rotating material around the protosun compressed into a disc as a result of the angular momentum - this is the protoplanetary disc. The protoplanetary disc contained all the elements that would later form the planets, their moons, and all the other extraterrestrial elements in our Solar System [3].

The temperature at the inner parts of the protoplanetary disc was very high, because of its vicinity to the protosun, so only the most refractory elements could condensate. CAIs were formed in this region. CAIs were the first objects to condense out of the protoplanetary disc, and therefore the age of the Solar System is defined by their age. According to Al-Mg dating their formation occurred over a very short period, only a few thousand years [11]. Further out, as the distance to the protosun increased, the temperature was lower and it was therefore possible for the less refractory elements to condensate. This material gathered in small clusters and, when flash heated, they melted, forming chondrules. This formation process went on for millions of years. All of these different types of material accreted into larger objects and from then to protoplanetary objects.

Before the collapse, the nebula had been infused with short-lived (on an astronomical scale) isotopes produced in a nearby supernova, like *e.g.* ^{26}Al . This isotope has a half-life of ~ 0.72 Ma [9] so it quickly decayed to ^{26}Mg , producing large amounts of heat. At some point, the protoplanetary objects became so large that the heat could not escape from them quickly enough and the objects started to melt.

The now molten protoplanetary objects then started to differentiate - the siderophile elements (*i.e.* metals) formed a core and the lithophile elements (*i.e.* the elements in stone phase) the mantle. This core/mantle differentiation continued as long as a sufficient amount of heat was generated from the decay of ^{26}Al .

Other protoplanetary objects that either accreted later or in a reservoir with a low ^{26}Al concentration were not completely molten and therefore remained undifferentiated. The accretion and collision between the protoplanetary objects continued until only relatively few protoplanets were left, together with the debris from the violent collisions and the smaller accreted objects that did not form protoplanetary objects. The material left over from the formation process would later become what we know as asteroids. Most of these are located within the asteroid belt between Mars and Jupiter at approximately ~ 3.5 AU [3]. Most of the meteorites that arrive on Earth come from asteroids, except a few that come from the Moon or Mars.

2.1.3 The Allende meteorite

The Allende meteorite is a carbonaceous chondrite of type CV3. It fell in Mexico near the town of Allende in February 1969 and it is the largest chondrite found on Earth, with an estimated weight between 2-5 tonnes [3].

It is the most studied chondrite and for many years it was our only source of CAIs. However, the Allende meteorite is no longer considered one of the most pristine chondrites. It was initially thought that the olivine that coats the chondrules and is a major matrix mineral in many CV3 chondrites were formed in an oxidizing nebula gas. However, transmission electron microscopy studies of Allende's matrix done by Adrian J. Brearley in 1999 [12] and thermodynamic analysis done by *e.g.* Krot et al. in 2004 [13] both indicated that metamorphism at temperatures above $\sim 200^\circ\text{C}$ was the cause of the alteration, not nebula processing. In 2005 Lydie Bonan et al. [5] determined the thermal metamorphism grade of nine CV3 chondrites, Allende included, by using several metamorphic tracers *e.g.* Raman spectroscopy (to determine the maturity of the organic matter in matrix), presolar grain abundance, and noble gas abundance. They discovered that Allende is a CV3.6 chondrite that had been heated to $550\text{-}600^\circ\text{C}$ and is thus one of the two most metamorphosed CV3 chondrites [5, 9].

Studies have concluded that the two most abundant elements in CV-chondrites are oxygen (37%) and iron (23.5%) [14].

2.2 Tomography

Tomography is the technique of a beam probing a sample by measuring how much of the incident beam passes through while turning the sample 180° - 360° . Think of it as taking a 2D picture of the surface perpendicular to the beam, turning the sample a little bit, taking another 2D picture and so on. What you end up with is a value depending on the transmission for each voxel, the 3D equivalent of the 2D pixel, representing the physical characteristics of that part of the sample – and by setting a colourscale, you get a 3D representation of your sample.

In tomography, you look at 2D slices of the sample which gives 1D data for each angle, as illustrated in figure 4. Then you apply the Radon transform to these in order to get a tomographic image.

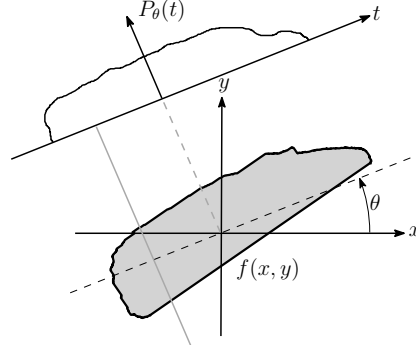


Figure 4: The projected 1D data, $P_\theta(t)$, of a 2D slice, $f(x, y)$, at an angle θ . $P_\theta(t)$ will be further explained in section 2.2.2.

The process of making a tomographic image naturally requires that the beam *can* pass through the sample. If the beam is halted at a certain place by an impenetrable material, the region behind this will be blacked out on the 2D image. Of course, when the sample is turned, the region again becomes visible from the other angles; but if the entire sample (or just the area perpendicular to the beam) is made of material impervious to the certain kind of beam applied, the images will be blank, as no information about the material is unveiled.

If all the different elements in the sample have roughly the same attenuation, tomography will not yield useful information, as the entire tomographic image would be the same colour.

2.2.1 Attenuation

When a particle meets an atom, three different things can happen: it can be scattered, absorbed, or transmitted.

In tomography, the interest lies in transmission: how much of the beam passes through a given sample. The damping, or attenuation, of the beam depends on the sample material of which the chosen physical characteristics varies with the type of beam.

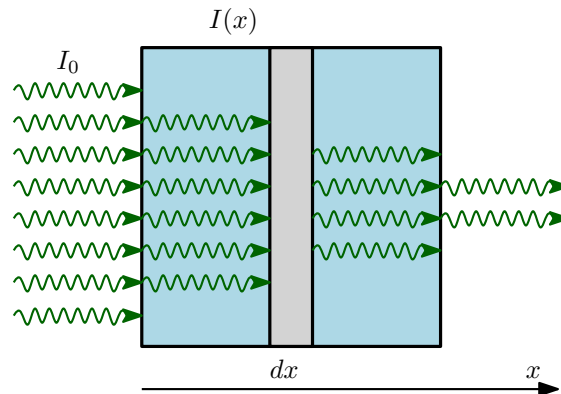


Figure 5: Attenuation for a slab of thickness dx .

The attenuation at a depth x from the surface through an infinitesimal sheet of thickness dx is defined as μdx , where μ is the absorption coefficient, see figure 5. The intensity of the sample thus changes accordingly with μ as

$$-dI = I(x)\mu dx \quad (2.1)$$

which, with rearranging of the terms, is a differential equation. Defining the incident beam I_0 by the initial condition $I(x=0) = I_0$ and assuming μ is a constant gives the equation for the intensity of the beam

$$I(x) = I_0 \cdot e^{-\mu \cdot x} \quad (2.2)$$

as a function of the thickness of the slab, x , and the absorption coefficient, μ . Thus the transmission through a sample is given by

$$T = \frac{I(x)}{I_0} = e^{-\mu \cdot \xi} \quad (2.3)$$

where ξ is the thickness of the sample. The absorption coefficient is a physical property of the sample's matter and can be found experimentally by comparing the beam intensities with and without the sample, but is also given by

$$\mu = \frac{\rho_m \cdot N_A}{M} \cdot \sigma_{a,s} = \frac{n \cdot N_A}{V} \cdot \sigma_{a,s} \quad (2.4)$$

where ρ_m is the mass density, M the molar mass, N_A Avogadro's number, n the number of moles, and V the volume. $\sigma_{a,s} = \sigma_s + \sigma_a$ and is the cross section per atom, which can be seen as the effective area of the nucleus (or atom) perpendicular to the affected beam. The cross section can be either absorption, σ_a , scattering, σ_s , or both, depending on which physical reactions occur.

All of the above applies to homogeneous samples, but in order for tomography to work, μ must not be constant. Solving equation 2.1 under the assumption that μ is not constant you get:

$$I(\xi) = I_0 \cdot e^{-\int_0^\xi \mu(x) dx} \quad (2.5)$$

Practically, however, instead of evaluating a line integral, an estimate of the average μ can be calculated as the sum-edition of equation 2.4:

$$\mu = \sum_i \frac{\rho_m \cdot N_A}{M_i} \cdot \sigma_{(a,s),i} = \sum_i \frac{n_i \cdot N_A}{V_{sample}} \cdot \sigma_{(a,s),i} \quad (2.6)$$

For a composite material this becomes the sum of the individual elements', i , contribution to μ , thus making ρ_m the different elements' mass compared to the entire volume of the sample.

μ can also be calculated for a composite material using the following equation:

$$\left(\frac{\mu}{\rho_m} \right)_{mixture} = \sum_j w_j \left(\frac{\mu}{\rho_m} \right)_j \quad (2.7)$$

where ρ_m is the density, j is the number of different elements, w_j is the weight percentage of the j 'th component or element, and ρ_m/μ is the mass absorption coefficient.

2.2.2 Radon transformation

In 1917 the Austrian mathematician Johann Radon published a paper in which he solved the problem of how to reconstruct a function from its projected data [15]. For an object represented by the 2D function $f(x,y)$, the projected 1D function $P_\theta(t)$ along the line $t = x \cos(\theta) + y \sin(\theta)$ is

$$P_\theta(t) = \int_{-\infty}^{\infty} \int_{-\infty}^{\infty} f(x,y) \delta(x \cos \theta + y \sin \theta - t) dx dy \quad (2.8)$$

This is the Radon transform for the object $f(x,y)$. In tomographic experiments $P_\theta(t)$ originates from the measured value; equation 2.8 is actually a more general version of equation 2.5, where $f(x,y)$ is the value of interest as $f(x,y) = \mu(x,y)$, where the δ -function ensures that $P_\theta(t)$ is in the right direction. In order to render the original object from the projection, two mathematical tools are needed - the Fourier Slice Theorem and the filtered backprojection algorithm [16].

The Fourier Slice Theorem takes the Fourier transform of the projection, $P_\theta(t)$, and gives the Fourier transform of the object, $f(x,y)$, along a line with an incline of θ [15].

The filtered backprojection algorithm converts the backprojection when taken at a finite number of angles, θ , and converts it back into a 2D object. It depends on the geometry of the beam, *i.e.* whether it is a cone or a fan beam [15,16]. In a cone beam the rays are divergent, forming a cone, and the fan beam is a 1D beam shapes like a rectangle.

2.2.3 Tomography Geometry

The field of view can be calculated using simple trigonometry. Imagine that the beam is emitted from a point-source, P , a distance L_d from the detector. The sample is placed between the source and detector at a distance L_s from the source, as in figure 6(a).

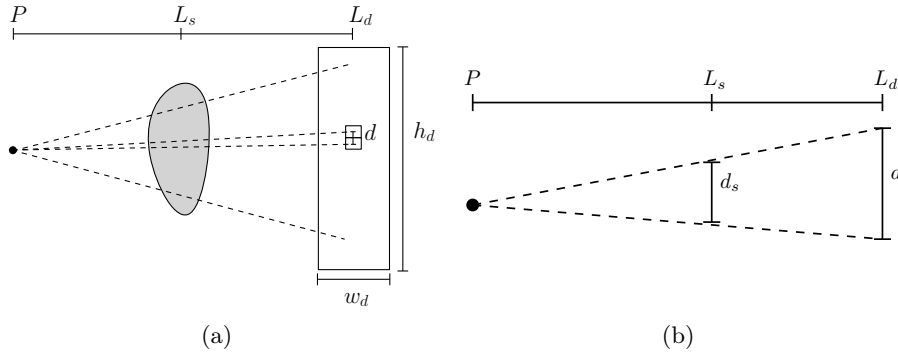


Figure 6: Schematic drawing of (a) X-ray transmission through a sample and (b) the angle between two photons, where d_s is the resolution.

The field of view is the maximum span that can be detected at a given distance. The outer ranges of the beam and the source form an isosceles triangle, therefore the following equation can be given for the field of view D :

$$D = \begin{cases} h_d \frac{L_s}{L_d} & \text{for the height} \\ w_d \frac{L_s}{L_d} & \text{for the width} \end{cases} \quad (2.9)$$

where h_d and w_d is the height and width of the detector, respectively.

The resolution can be determined in a similar way when we assume the angle between the photons is sufficiently small so they too form an isosceles triangle as seen in figure 6(b). The measurement resolution d_s is given by

$$d_s = \frac{d \cdot L_s}{L_d} \quad (2.10)$$

where d is the detector resolution, given by the size of each pixel in the detector.

2.2.4 X-ray tomography

X-rays were discovered by Wilhelm C. Röntgen in 1895 [17]. They are electromagnetic waves with wavelengths in the order of 1 \AA and energies in the same order of magnitude (keV) as the binding energy of a K-shell electron to an atom. The penetration depth of X-rays is often much longer than that of visible light because the wavelength of X-rays is much shorter. The attenuation of a X-ray

beam through a sample varies in general as Z^4 and is the basis of normal radiographic images; Z is the atomic number *i.e.* number of protons.

The X-ray absorption process is known as photoelectric absorption, given by the linear absorption coefficient μ . Basically, an X-ray photon is absorbed by the electron cloud around a atom and the excess energy is transferred to an electron. Photons with energies above the binding energy will expel an electron from the atom with a certain probability, leaving it ionized. Generally the probability of absorption decrease with increasing photon energy [17].

However, as the energy increases, so does the possibility of scattering of the photon and the attenuation is no longer due to just absorption. When X-rays are scattered they interact either elastically or inelastically with the electrons. In inelastic scattering, Compton scattering, an outer electron and the incident beam collides, separating the electron from the atom and lowering the rays energy. Because of the principle of conservation of momentum, the beam continues at a angle compared to the incident beam, described by the Klein–Nishina equation [18]. Elastic scattering is known as Thomson scattering; here no electron is expelled and the beam continues with the same energy, but at an angle up to 90° [17].

For energies up to about 50-100 keV, absorption dominates. Above this value Compton scattering has to be considered up to 5-10 MeV, where pair-production becomes the primary contributor to the attenuation [19].

Whereas the absorption cross section varied as Z^4 , Compton scattering cross section varies as Z . An illustrative example of the importance of considering the mechanisms behind the attenuation can be seen in figure 7, where four common minerals' attenuation curves are shown. Due to the difference in their proportionality to Z at different energies, the low X-ray energies are more sensitive to differences in sample composition than higher energies, where the difference between similar materials can no longer be distinguished.

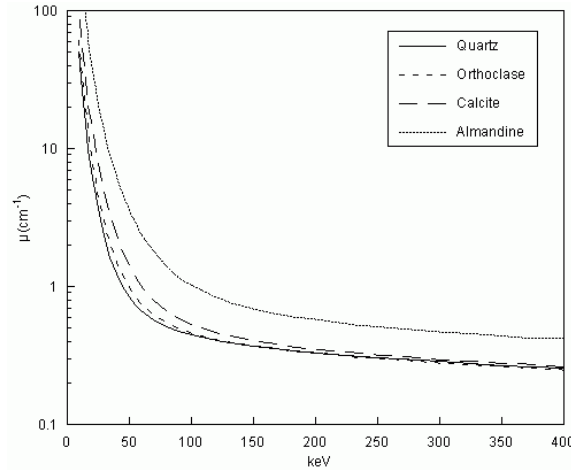


Figure 7: Shown are the attenuation curves for the minerals quartz SiO_4 (solid line), orthoclase KAlSi_3O_8 (small dashed line), calcite CaCO_3 (big dashed line), and almandine $\text{Fe}_3^{2+}\text{Al}_2\text{Si}_3\text{O}_{12}$ (points). At low energies, the coefficient is different for all the minerals. Around ~ 125 keV, the curves for quartz and orthoclase meet, while the convergence between quartz and calcite happens at a higher energy. [19]

At low energies, quartz and orthoclase, which has similar densities, have different attenuation coefficients because of the presence of potassium in orthoclase. As the energy increases, the attenuation coefficients converge, and above about 125 keV, where Compton scattering is the dominating mechanism, quartz is the more attenuating, owing to its slightly higher density. Due to the high content of calcium in calcite, it is more attenuating than quartz and orthoclase, though only slightly denser, and reaches similar coefficients as quartz at higher energies. Almandine, high in both density and elements

with high Z , is distinguishable at all energies throughout.

The energy of the X-ray beam used in experiments is generally denoted by the output energy, but is actually a broad spectrum with energies ranging from zero to the peak value with varying intensities; the distribution is described by the Bremsstrahlung spectrum [16]. The effective energy is below the maximum energy of the X-ray source and can be calculated experimentally by comparing the theoretical $\mu(E)$ value with the one found in the experiment, giving $\mu(E) = \mu_{exp} \Rightarrow E_{eff}$.

Because the beam is a spectrum of several energies, an effect called beam hardening can distort the data. Beam hardening appears because the average energy of the X-ray beam will increase on its way through the sample; the lower energies will be preferentially removed from the beam, lowering the overall intensity but make the average energy increase. As a result, the change in absorption coefficient may stem from the change in the average energy and not in density.

The effect of beam hardening is that the edges and middle of an object will have higher and lower absorption coefficients, respectively, than they would otherwise. The effect becomes larger the longer the beam travels.

2.2.5 Neutron tomography

Neutrons were discovered in 1932 by James Chadwick; their existence had been hinted at, since Rutherford showed that the mass of the atom for most elements was twice that of their proton number [20]. The neutron particle's ability to mediate chain reactions by radioactive decay, and thereby nuclear fission, was quickly utilized with both peaceful and lethal outcome.

The neutron is one of the fundamental particles that together with protons and electrons make up the atoms. Like with X-rays, the wavelength is similar to atomic distances, $\lambda_{th}=1.798 \text{ \AA}$ (or a velocity of $v_{th}=2200 \text{ m/s}$) [21], but corresponding to a lower energy than X-ray, 25 meV: the so-called 'standard' thermal neutrons.

Whereas X-rays interact with the electrons, neutrons probe the nucleus itself. For that reason, neutron analysis depends on other elemental characteristics of the sample than X-ray and as such give a different tomographic image. As opposed to X-rays, the attenuation's correlation with these elemental characteristics – being Z , N , or another fundamental atomic property – is of yet unknown to physics, and the cross sections are thus experimentally determined values.

The attenuation of neutrons happens because of the same general mechanics as for X-rays, absorption and scattering, but with a different energy dependency. Neutrons scatter readily with a constant value unaffected by the beam energy. The effective absorption cross section, however, does depend on energy in concordance with the following equation:

$$\sigma_a = \sigma_{a,th} \cdot \frac{\lambda}{\lambda_{th}} \quad (2.11)$$

where $\sigma_{a,th}$ is the table value of the thermal absorption cross section of isotope i . As with X-rays, the higher the energy, the less absorption occurs.

The absorption of a neutron into the nucleus leaves the atoms slightly radioactive, and a decay period is necessary after an experiment. The scattering of the neutrons, as for X-rays, can be both coherent and incoherent, where, to a first order approximation, only the latter is important when considering the attenuation.

Coherent scattering occurs due to interference between the neutrons scattered from neighbouring atoms, and makes them scatter at a certain angle, instead of with a random value, like for incoherent. This is the basis for the related technique of neutron scattering, which seeks to minimize the background of incoherent scattering in order to study the sample's characteristics by their coherent scattering angle [21].

Neutrons are able to probe not only the surface of a sample, but also the interior, even of bulky samples up to tens of centimeters in thickness, because the interaction between neutrons and most elements is quite weak. Just a few distinct elements have high cross sections, and among the elements readily present in minerals, hydrogen and a few metals are the only ones contributing.

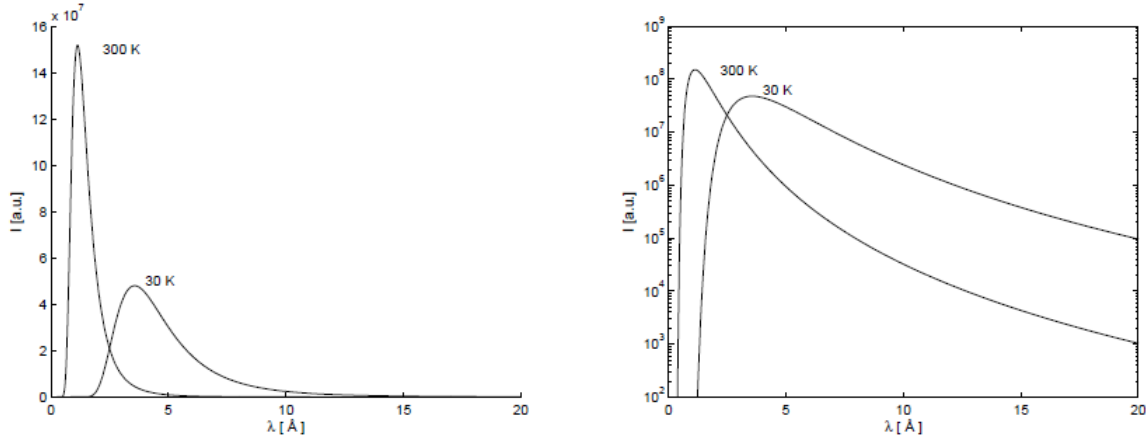


Figure 8: Two Maxwellian energy distributions for thermal, 300 K, and for cold, 30 K, neutrons, plotted with both normal and semi-logarithmic axis to show the behaviour at long wavelengths [21].

Like X-rays, the energy of the neutron beam is a continuous spectrum. It is approximated by a Maxwellian distribution depending on the temperature of the neutron moderator, of which two are illustrated in figure 8. While the energy varies for X-ray tomography, neutrons are normally described by wavelength. Beam hardening does occur, but it is a secondary effect.

2.3 Tomography of chondrites

X-ray tomography has been done by *e.g.* Jon M. Friedrich, who did X-ray tomography on a piece of Allende [22]. Looking at X-ray attenuation within small 1-3 cm³ chondrite volumes, he was able to classify chondrites by the spatial variation of the minerals contained within them. He found that the fine-grained matrix of Allende could be clearly distinguished from the chondrules and refractory elements, which were both considerably darker in the tomographic images, as can be seen on figure 9.

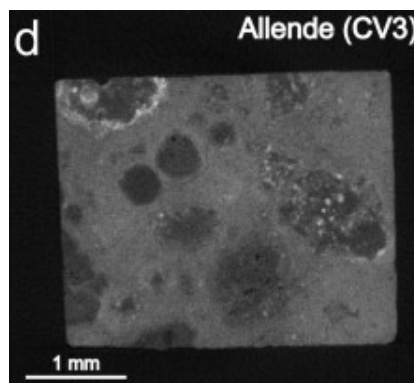


Figure 9: Synchrotron X-ray slice from the reconstruction of a small part of Allende collected at a resolution of 16.6 μm voxels, as taken from Friedrich's article. The matrix can be easily distinguished from the darker chondrules and Calcium Aluminium-rich Inclusions [22].

However, the petrological types of chondrites cannot be readily decided from the tomographic images. By using grey-scale statistics and the so-called Betti numbers, which describes the homology (a mathematical topological tool) of components of interest and can be used to investigate how the morphology changes with metamorphism, he was able to distinguish between different petrologic types for three

different ordinary chondrites of type L. He was also able to separate the L-chondrites from Allende (*i.e.* a CV-chondrite).

D.S. Ebel and M.L. Rivers have also worked much on X-ray tomography of meteorites and have also done experiments on a piece of Allende [6]. They, like J.M. Friedrich, found that the matrix could easily be distinguished from the chondrules and CAIs on X-ray tomographic images. Allende matrix has a relatively high, uniform iron-oxide content, which gives a high contrast relative to clasts, and thus it was possible for them to isolate chondrules/CAIs from matrix at a high confidence level.

Ebel and Rivers concluded that 3D sample analysis is the preferred first step in approaching all rare extraterrestrial samples, even at low resolution, as tomography can bring interesting elements to light and help choose where it is best to slice a rare sample for surface chemical analysis. Not only does tomography yield a set of images, it also gives valuable information which thin slices of a stone cannot. 3D images are optimal for investigation of the way meteorites are put together (*e.g.* determining the matrix-chondrule-CAI relationship) as well as studies of the size and shape of chondrules and CAIs.

3 Method

3.1 Our piece of the Allende meteorite

The piece of Allende we wished to examine weighs 25.25 g, and measures $11 \times 41 \times 38 \text{ mm}^3$. Photos of the meteorite from two different angles is shown in figure 10. Photo 10(a) shows a part of our sample which have not been altered during the fall through the Earth's atmosphere, and one can clearly see the matrix, chondrules, and CAIs. Photo 10(b), however, is part of Allende's fusion crust, *i.e.* it was altered by melting when entering the Earth's atmosphere.

The piece has previously been examined by neutron tomography at PSI in Switzerland in 2005, as mentioned earlier, where an interesting inclusion was discovered. The inclusion should be situated inside the green circle, shown in picture 10(a).

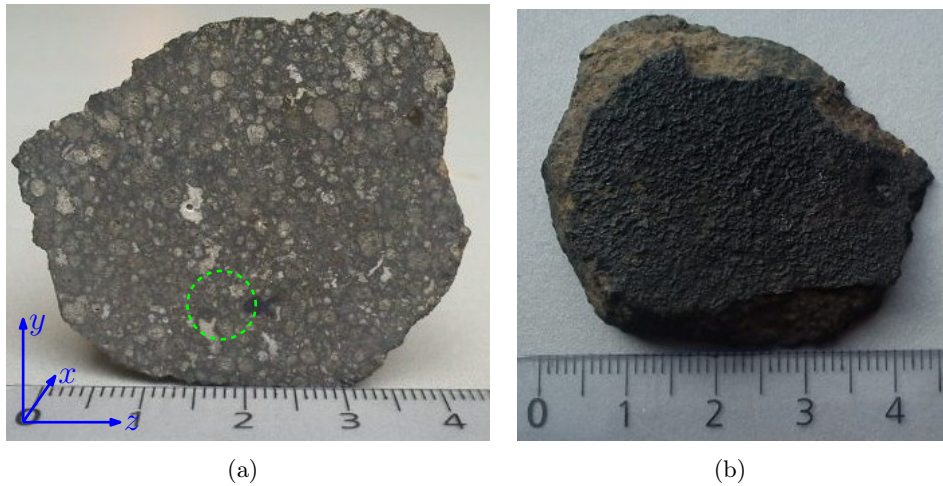


Figure 10: Pictures of our Allende sample from different angles. The previously discovered inclusion is located inside the green circle in photo (a).

3.2 X-ray tomography

3.2.1 Beam Attenuation

X-rays are normally used to investigate soft or biological tissue (*e.g.* your luggage at the airport or you, when going to the hospital with a broken arm), and not stones or meteorites. Hence, in order

to know if this was even possible at a reasonable range of beam energies, a preliminary calculation of the beam attenuation had to be done. The rule of thumb is that the transmission, T , needs to be a minimum of 10% to get a working tomographic image.

The attenuation of X-rays happens when the photons react with the electron cloud, and hence a formally fully correct treatment of the attenuation coefficient should actually be based on the mineral composition of the meteorite, and not the elemental as the configuration of the electrons is, of course, determined by the molecular structure. However, the corrections are extremely small, and at any rate, the sheer number of minerals in stones is so vast that a mapping of the minerals would not be plausible. As an approximation, the following is applicable.

First, we calculate the linear absorption coefficient, μ , using equation 2.7. A CV-chondritic meteorite like Allende contains just about every natural occurring element in varying amounts. The weight percentage and mass absorption coefficient of the 10 most abundant elements is given in table 1, along with each element's contribution to the average μ .

Although the dampening effect of X-rays increases as we go further in the periodic table, the rest of the 92 elements constituting CV-chondrites are found in so small quantities, ppm or even ppb, that their contributions to μ are not significant. Thus, when calculating μ , we have chosen to only use the 10 most abundant elements.

A standard value of grain density for CV-meteorites at 3.5 g/cm³ along with 11% empty space [23] was used, giving an effective density of 3.1 g/cm³, resulting in a μ -value for the whole stone of 0.43 cm⁻¹ at 170 keV.

Z	Element [14]	wt% [14]	μ/ρ_m [cm ² /g] [24]	μ [cm ⁻¹]
1	H	0.28	0.244	0.0021
6	C	0.53	0.127	0.0021
8	O	37.0	0.126	0.144
12	Mg	14.3	0.127	0.057
13	Al	1.68	0.133	0.0069
14	Si	15.7	0.139	0.067
16	S	2.20	0.139	0.0095
20	Ca	1.84	0.152	0.0087
26	Fe	23.5	0.169	0.123
28	Ni	1.32	0.169	0.0077
Total		98.4	0.138*	0.43

Table 1: Table of wt%, μ/ρ , and μ . The μ/ρ_m values are for an energy of 170 keV. Elements whose fraction is given in ppm or lower have been ignored. *Weighted average.

The transmission as a function of the beam's energy is illustrated in figure 11 for energies between 2 and 440 keV, calculated using equation 2.3. We see that for X-ray energies below about 100 keV, no tomography is possible for our sample.

As an example, the transmission through each side of the meteorite at an energy of 170 keV is

$$\begin{aligned} T_{11mm} &= e^{-\mu \cdot 1.1cm} = 0.624 \\ T_{38mm} &= e^{-\mu \cdot 3.8cm} = 0.196 \\ T_{41mm} &= e^{-\mu \cdot 4.1cm} = 0.172 \end{aligned}$$

Thus tomography is definitely possible for an energy of 170 keV, as more than 10 % is transmitted through each side.

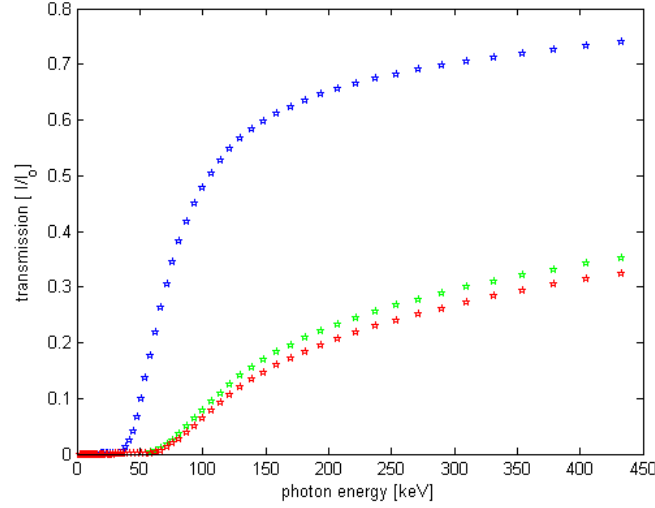
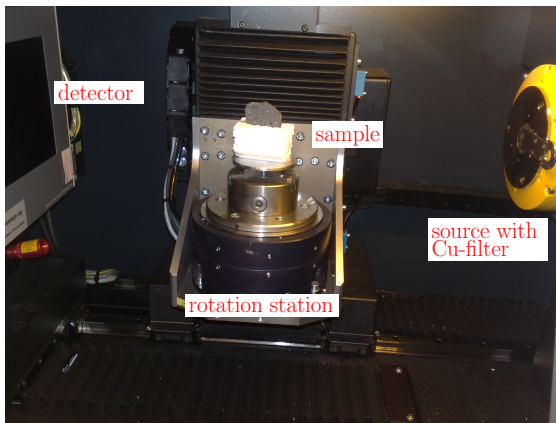


Figure 11: *Calculated transmission of X-rays as a function of energy for our sample; blue dots show the transmission through side x (11 mm), green through side y (38 mm), and red through side z (41 mm).*

3.2.2 Experimental setup

The experiment was conducted at Novo Nordisk in Hillerød on the phoenix Nanotom® X-ray machine. The detector in the Nanotom is a flat panel detector from Hamamatsu, with dimensions of 2316×2316 pixels and a pixel size of $50 \mu\text{m}$ [25].

X-rays are emitted from the source using the following process: The source consists of a filament (a cathode) and a metal target (an anode). A current is sent through the filament and electrons are released; they are then accelerated by an applied high-voltage electric current. When the electrons hit the target, they lose their energy by excitation, radiation, or ionization of the atoms in the target material – only about 1% of the energy generated is emitted as X-rays. The X-ray photons are emitted in the same direction as the electron beam [26]. The output spectrum is a continuous spectrum of X-rays, known as the Bremsstrahlung spectrum [16]. The limit of the photon energy in the spectrum is set by the potential difference over the filament and the target.



(a)



(b)

Figure 12: *The setup of the X-ray experiment at Novo. Picture (a) shows the stone's placement inside the machine – securely placed in polystyrene on a rotating stage. Picture (b) shows a larger view of the nanotom X-ray machine.*

The meteorite was placed securely in polystyrene, as seen at figure 12, because polystyrene has a very

low X-ray attenuation coefficient. A 0.5 mm Cu-filter was placed in front of the source in order to remove the smallest energies and thus reduce beam hardening by absorbing energies up to 25 keV completely. A 170 keV X-ray beam from a tungsten anode was used. The distances between sample, detector, and source was $L_d=500$ mm and $L_s=250$ mm, *i.e.* the field of view was about 60×60 mm² and the data have a magnification of 2 with a voxel size of $25 \mu\text{m}$.

A schematic drawing of the rays path from the source, through the sample and to the detector can be seen in figure 13.

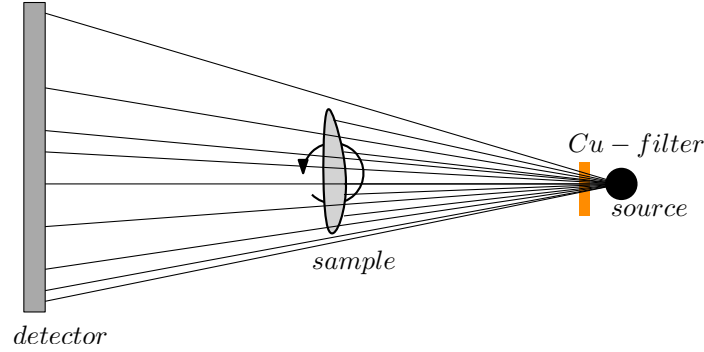


Figure 13: Schematic drawing of the ray's path from the source to the detector. A Cu-filter is placed in front of the source to reduce beam hardening.

Before the experiment began, the filament was adjusted so the electron spot was on the target and the target was centered. Then the machine was calibrated in order to remove unwanted noise from the image.

We chose an output of 1100 pictures. The machine took 3 pictures at the same angle, saved the average of the first two and then skipped one picture. Each picture took 1 s, therefore the experiment lasted for about 60 minutes. The sample was rotated 360° at increments of 0.33° between each final picture.

3.2.3 Reconstruction

We compared the first and last picture to see if the meteorite had moved during the experiment. The stone did not move during the rotation, so no correction was needed.

To reconstruct and compile the data, the program `datos|x acquisition` [27] was used. The Nanotom uses a cone beam, so the filtered backprojection algorithm for a cone beam was used. Beam hardening was set to 9 (this is an option in the program that corrects for beam hardening) and the image was cut so only $2/3$ of the field of view would be reconstructed. Thus the reconstructed pictures are $540 \times 862 \times 954$ voxels. The program took about 10 minutes to run, for the whole stone in half-resolution. In full resolution, the image was split up into a top and a bottom half and the program took about 30 minutes to run for each half.

In the end, we had 6.76 GB of .raw datafiles, an image file type containing minimally processed data. One file with the whole stone in half-resolution (*i.e.* with $50 \mu\text{m}$ voxels) of 846 MB, as well as two files in full resolution; one with the bottom of the stone of 2.97 GB and one with the top of 2.96 GB.

Unfortunately, the reconstructed data in full resolution turned out to be very grainy, and the datafiles were too big for us to run on our own computers anyway, so we chose to use the dataset with the whole stone in half-resolution for all further investigation. We also have the whole stone as Tiff-pictures and a .vol file, both the same size as the .raw file.

3.3 Neutron tomography

3.3.1 Beam attenuation

Although we know that neutron tomography is possible since our piece of Allende has already been examined with it, we do the same calculation of its average μ and the transmission as we did for X-rays.

As opposed to X-rays, the use of the individual elements *are* formally correct for neutrons, as the particles react with the nuclei which do not sense the presence of each other.

Whereas we only used the 10 most abundant elements when calculating the X-ray attenuation coefficient, the situation with neutrons is a bit more complicated. The cross sections, σ , of neutrons has no correlation with the atomic number, and as such the elements of a CV chondrite present in only ppm or ppb cannot readily be excluded. Instead, we looked at *all* 92 elements and evaluated the order of magnitude of their individual contribution to μ .

Z	Element	N [10^{23}]	σ_{inc} [10^{-28}m^2] [28]	$\sigma_{a,th}$ [10^{-28}m^2] [28]	μ [m^{-1}]
1	H	0.422	80.26	0.3326	41.7
6	C	0.0671	0.0010	0.00350	0.00037
8	O	3.52	0.000	0.00019	0.00082
12	Mg	0.895	0.080	0.063	0.16
13	Al	0.0947	0.0082	0.231	0.028
14	Si	0.850	0.0040	0.171	0.18
16	S	0.104	0.0070	0.53	0.069
20	Ca	0.0698	0.050	0.43	0.080
26	Fe	0.640	0.40	2.56	2.33
28	Ni	0.0342	5.20	4.49	0.41
Cl	0.00107	5.3	33.5	0.066	
27	Co	0.00165	4.8	37.18	0.087
48	Cd	4.73E-7	3.46	25200	0.0015
64	Gd	3.92E-7	151	49700	0.024
Total					45.0

Table 2: N , σ_s , $\sigma_{a,th}$, and the contribution to μ for the 10 most abundant elements in Allende as well as the only elements of quantity in ppm or ppb with an attenuation coefficient of similar magnitude to that of the 10 first elements, for a wavelength of $\lambda=1.798 \text{ \AA}$. In the sum, we have only included individual values of μ higher than 0.001 m^{-1} .

The calculation was done using equation 2.6 and 2.11, and the necessary data as well as the results for the calculation at $\lambda = 1.798 \text{ \AA}$ can be found in table 2. A volume of the meteorite at $V=8.1 \text{ cm}^3$ found from the standard density of a CV chondrite and our own weighing of the stone was used, giving an attenuation coefficient of $\mu=45 \text{ m}^{-1}$.

From this we can see two things: the cross section-values varies to such a great degree that some of the most abundant elements contribute almost nothing, like carbon, while some of the elements present in just ppm or ppb actually reaches the same order of magnitude of μ , like chlorine.

However the most important information from the last column of table 2 is that all those elements' contributions are insignificant compared with that of hydrogen with a attenuation coeffecient 20 times and more greater; only iron comes even close.

Neutrons have almost the same attenuation coefficient as 170 keV X-rays, of 0.45 cm^{-1} and 0.43 cm^{-1} respectively, when only including contributions higher than 0.001 m^{-1} .

The transmission through each side of the stone was as for X-ray calculated using equation 2.3. The

results for wavelengths between 1-5 Å can be seen in figure 14, confirming that neutron tomography is indeed possible.

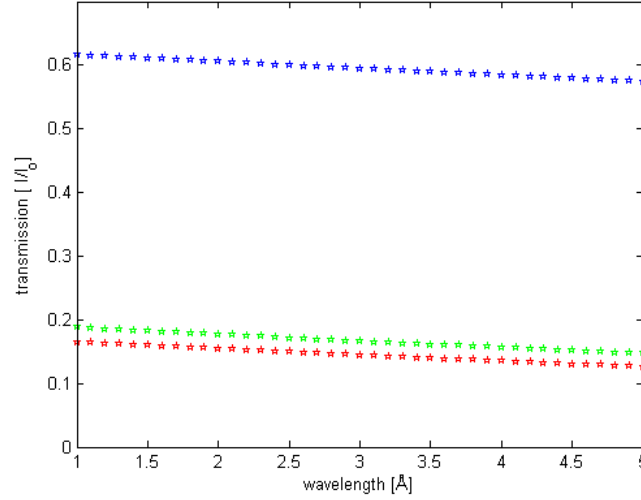


Figure 14: *Neutron transmission as a function of wavelength. Blue dots show the transmission through side x (11 mm), green through side y (38 mm), and red through side z (41 mm).*

3.3.2 Experimental setup

Neutron facilities are relative sparse, there are only about 8-10 places in the world where neutron tomography is possible, in comparison to X-ray where they are practically everywhere.

The neutron experiment was conducted at PSI in Switzerland using the NEUTRA beamline. We did not conduct the experiment ourselves, as it was not possible to schedule the beamtime in advance. Due to the rarity of the stone, we transported it to PSI ourselves and left it in the custody of Christian Grünzweig, PSI Switzerland, to conduct the experiment when beamtime was available.

NEUTRA uses a continuous spallation neutron source called SINQ. An intense 1 GeV proton beam is guided into the spallation source where it hits a target made of lead bars. This collision excites the lead nuclei to a higher energy level which is then released by evaporating neutrons; this is called a spallation reaction. SINQ will on average generate ten neutrons for each proton that hits the lead target [29]. When the neutrons leave the target, they have a speed of about 20,000 km/s *i.e.* an energy of ~ 2.1 MeV [29]; this velocity is too high for experimental use and the neutrons are therefore slowed down by passing through a moderator, in this case heavy water [30]. The neutrons now have the same velocity as the water molecules, continuously distributed around ~ 2200 m/s [29] and are now called thermal neutrons. The distribution at 300 K can be seen in figure 8.

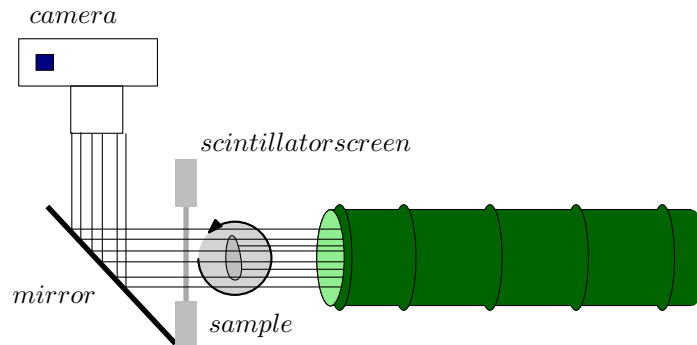


Figure 15: *The NEUTRA beamline of PSI; schematic drawing of the beam's path from the source to the detector.*

In order to protect the scientists from neutrons and gamma rays with very high energy, which cannot be decelerated in the before mentioned heavy water moderator, the source is surrounded by a 5 m thick shield made up of iron and concrete. The neutrons leave the moderator through a collimator that goes through the shield and ends at the rotating desk used in tomography, as can be seen in figure 15; the collimator alone is over 11 meters long [30]. The neutrons continue through the sample and on to a scintillator screen; where the neutrons are converted in to light via nuclear reactions in the scintillator material. The particles continue on to a mirror where the photons are deflected up to a camera where they are detected; the camera has 2048x2048 pixels with a pixelsize of 32 μm . The neutrons and gamma-rays continues until they are stopped by a beam catcher.

The stone was placed in aluminium foil on the rotation desk, as seen in figure 16. The distance between the sample and the source was 4700 mm and the distance between the source and the detector was 4760 mm, giving a field of view of 65×65 mm and a voxel size of 31.6 μm . Through the experiment took 10 minutes to run and the sample was turned 360° clockwise. A cone beam was used.

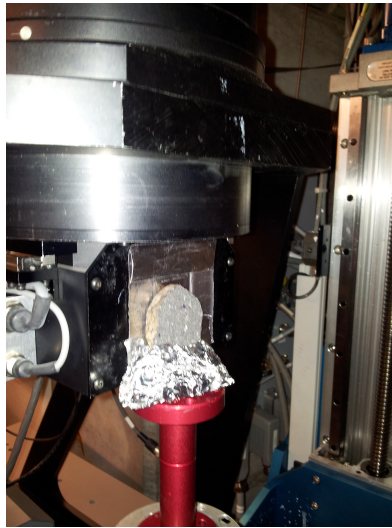


Figure 16: *Experimental setup of the neutron experiment at PSI, Switzerland. The experiment was conducted using the NEUTRA beamline.*

The data was reconstructed by David Mannes at PSI, Switzerland. No noise filter or beam hardening correction methods were used, which is why our data has a clearly visible ring effect, which is a reconstruction artefact, on all the images. We received 1370 Tiff-pictures (1.46 GB) on the 30th of May 2012.

The old neutron experiment was conducted at the same machine, but at a lower resolution; the data is shown and processed in appendix A.1.

4 Results

4.1 X-ray

Unfortunately, the Nanotom only returns reconstructed Tiff-images, therefore we have no transmission images but only reconstructed ones. In addition, the μ -value of each voxel is *not* given in cm^{-1} but in some arbitrary unit which can only be determined by conducting the experiment with something of known value next to the sample *e.g.* a metal cube. When this was discovered, we considered the possibility of doing another scan under the same conditions as the first one on a metal cube and comparing it with our tomographic image. However, during her master's thesis [16], Maria Thomsen, stud. Phd. at NBI, discovered while analyzing her data from an experiment conducted at the same machine, that the grayscale in the reconstructed volumes could change unpredictably between reconstructions.

Therefore the voxel values from two different scans cannot be compared. As our piece of the meteorite was now in Switzerland, awaiting neutron beamtime, it was not possible for us to redo the experiment. Therefore, all our μ -values are given in arbitrary units and it was not possible to convert them to another. For the same reason, we cannot calculate the effective energy, as described in section 2.2.4.

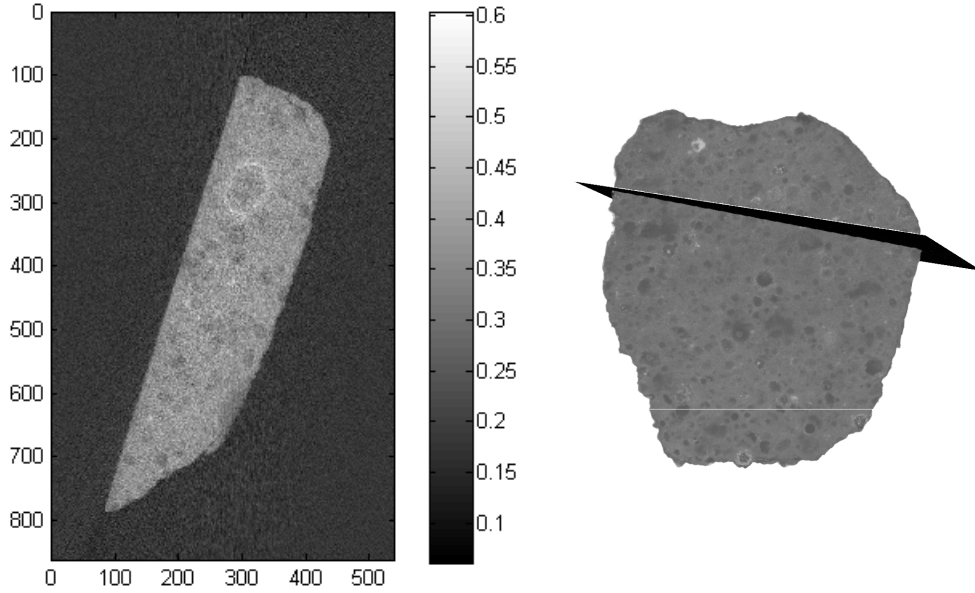


Figure 17: *Tomographic slice of the stone showing the inclusion that had previously been observed, using picture no. 460, and where the slice was taken.*

The slices do not follow the previously defined axis (figure 10(a)), as the orientation of the slices are of course determined by how the stone was placed during the experiment, and by the axis of compilement. The slices we have used throughout this paper are the ones given in the individual picture slices: of course the other two orientations are available, as the pictures can be made into a 3D image. Since the orientation of the slice can vary according to the above, we have for each experiment shown what way through the stone the slices are taken and at what angle.

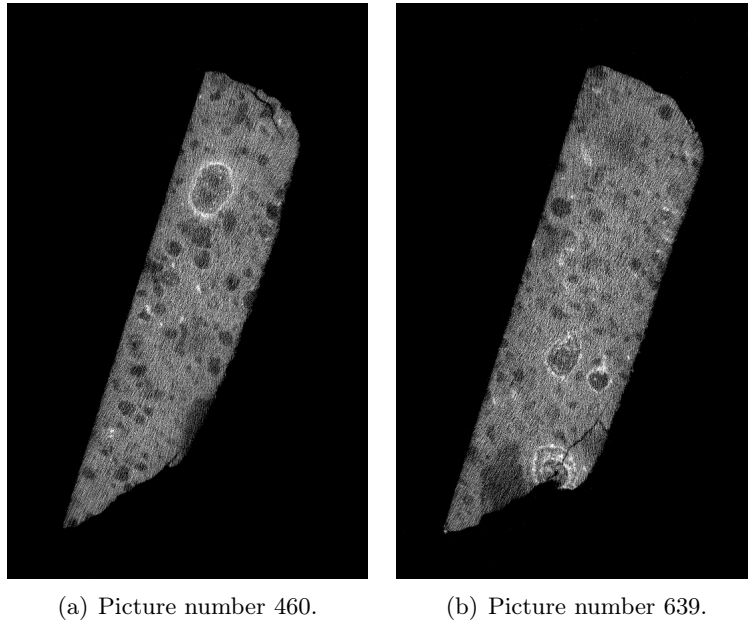


Figure 18: *Tomographic slices of the stone with enhanced contrast made in the program ImageJ, showing how the different elements are more distinguishable.*

A tomographic image of the stone can be seen in figure 17, showing the inclusion that had previously been observed, see figure 1. A colourscale has been added using Matlab version 2011a, showing which colours represents the different attenuation coefficient. The image contrast has not been altered, which is why the air is not black. Materials with low X-ray attenuation has a darker colour (*e.g.* the air) and materials with high X-ray attenuation are white (*e.g.* metals). The format of the data is 16uint which means the images have a colourscale between 0 and $2^{16}-1$. In order to convert the μ -values in our data to the right format, they are therefore divided by $2^{16}-1$.

To see the inclusions clearer, the contrast of the image can be altered; the best contrast for a tomographic image is when the air is completely black [22]. The altered image can be seen in figure 18.

Figure 19 shows a normalized histogram of the entire sample's μ -values, made in the open source program ImageJ. The air around the stone has *not* been removed from the tomographic image, which is why there are many pixels with values around 0.18. Inside the stone, there might be a few voxels with values around or below that of the air; but mostly the stone is represented by the μ -values above 0.25.

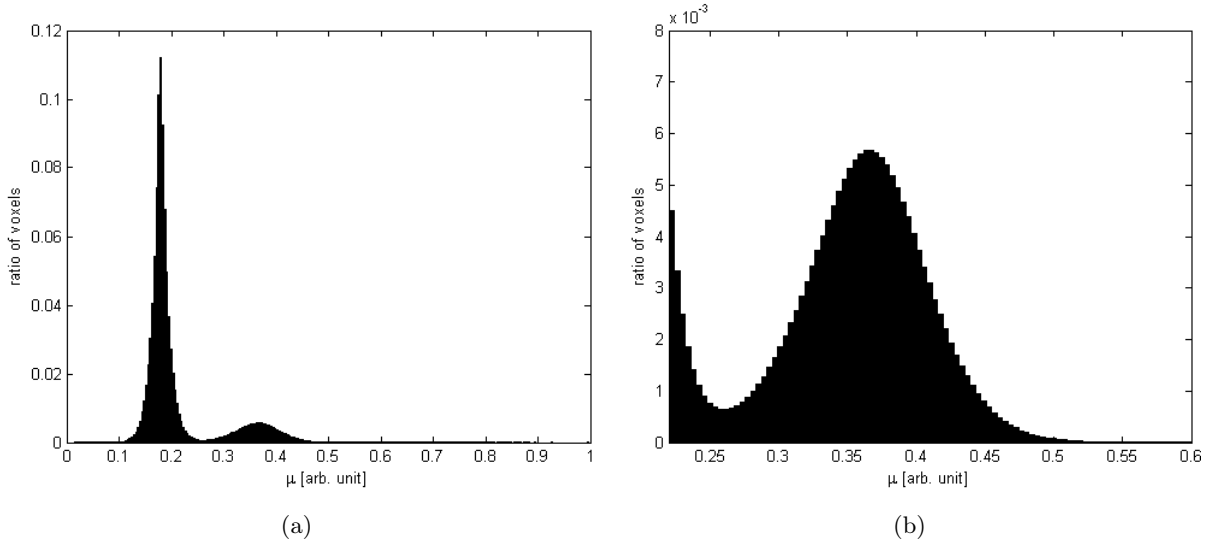


Figure 19: Normalized histogram for the entire x-ray tomographic image, made with ImageJ using 256 bins, where (a) shows the whole stone and the air and (b) is zoomed in on the stone's values. The air has a value of about 0.18 and the stone mostly has values above 0.2.

4.2 Neutron data

The output data from the NEUTRA beamline is in cm^{-1} ; however, the scaling of the reconstructed data is unknown. David Mannes, who reconstructed the data, chose a scale which gave the prettiest pictures; however, he does not know what this scale was and therefore we do not know what factor of cm^{-1} our voxel-values are. Thus our attenuation coefficients are, once again, in arbitrary units.

A Tiff-picture of the stone can be seen in figure 20, with a colourscale added in Matlab version 2011a. You can clearly see a quite large ring effect in the middle of the picture. The data are 8-bit.

Figure 21 shows normalized histograms of the entire sample. As can be seen in 21(a), most of the voxels have an attenuation coefficient of zero; this is because the air around the stone has not been removed from the tomographic image. Therefore, we have zoomed in on the stone's values in figure 21(b). The stone has a mean attenuation coefficient of about 35.

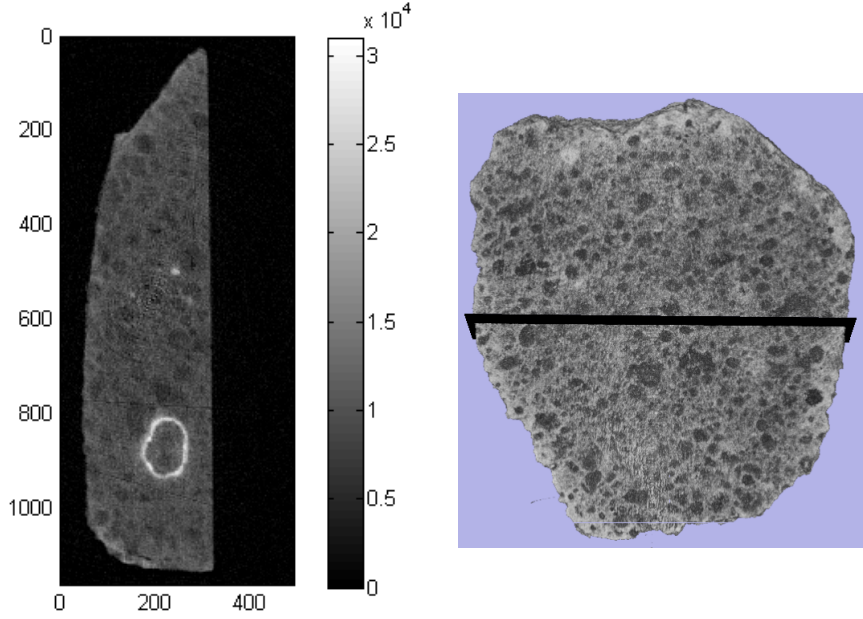


Figure 20: Neutron tomographic slice showing (a) the inclusion using picture 728 and (b) the orientation of the slice.

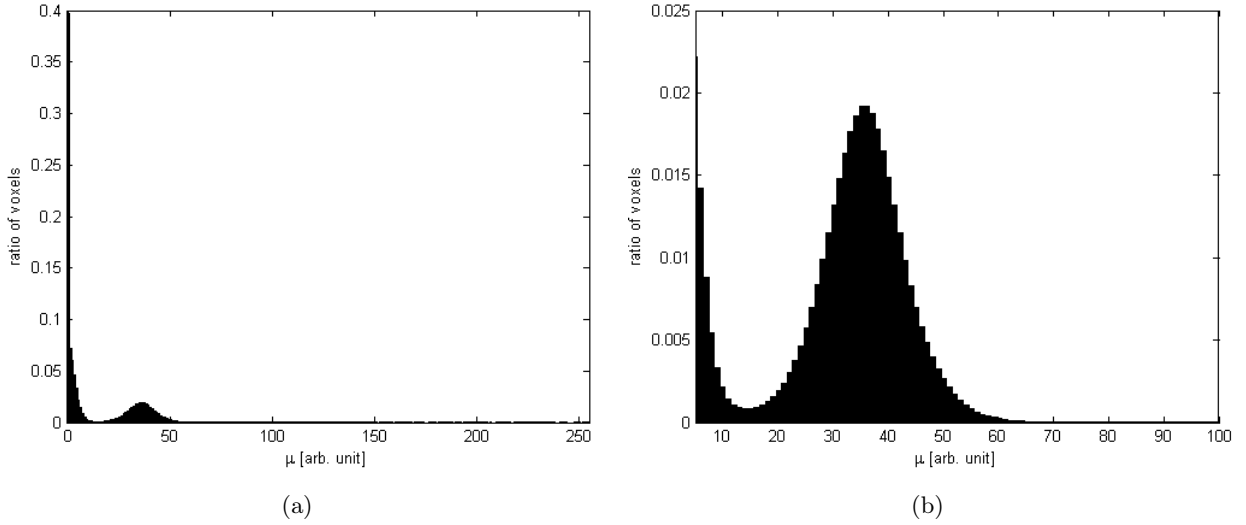


Figure 21: Normalized histograms for the neutron images using 256 bins where (a) shows the whole stone and the air and (b) is zoomed in on the stone's values.

5 Discussion

5.1 X-ray tomography

In the reconstructed tomographic image, figure 17, a great amount of darker inclusions can be clearly distinguished from the fine-grained matrix material. This is most likely chondrules; we will try to confirm this in section 5.1.1. Matrix is brighter so it attenuates the X-ray beam more than the chondrules, thus there are more metal in the former. This is consistent with what we already know about Allende, because even though the volatile elements are more abundant in matrix than in chondrules, matrix does not necessarily consist of less dense elements.

There are also several white rings; one is the inclusion we had previously seen on the neutron tomographic image. All the white rings are most likely rims on chondrules.

In earlier studies, chondrules were found to mostly have droplets of volatile minerals around the edges; we observe this on some of the chondrules in our images, but quite a few actually have continuous rims.

5.1.1 Comparison of stone and X-ray

Using the program Slicer we took a tomographic image right beneath the stone's surface. Comparing this image with one of the stone's surface in natural light, we should be able to confirm what we see in the X-ray image. The two compared pictures are shown in figure 22; larger images can be seen in appendix A.2.

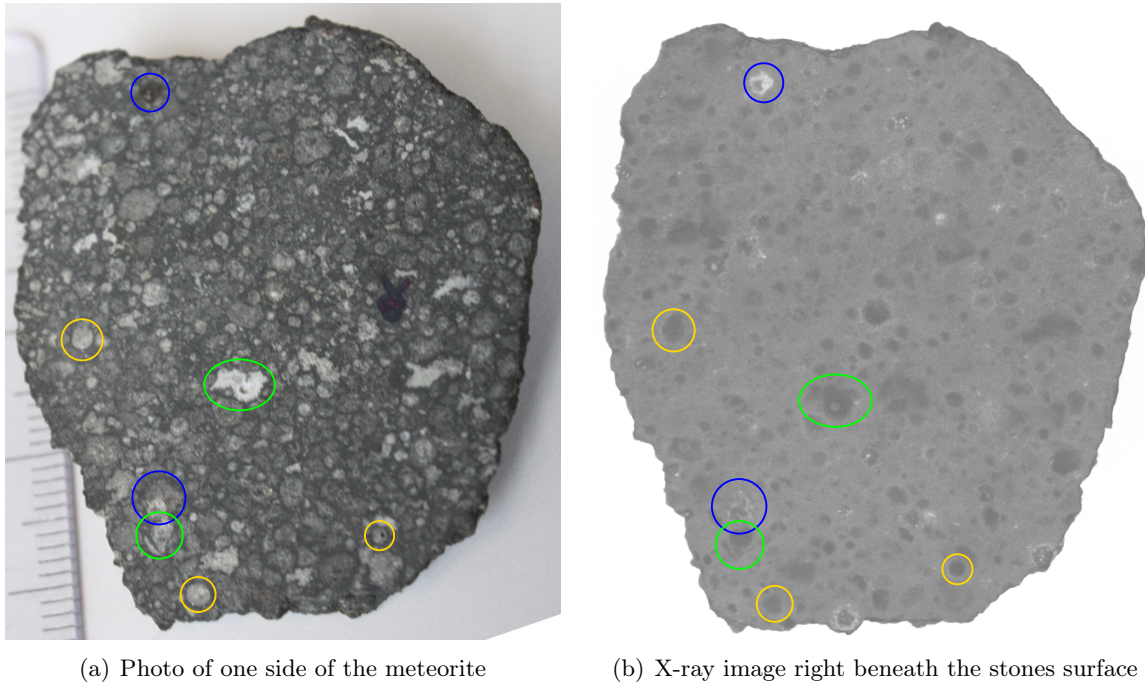


Figure 22: *The surface of the stone as seen by X-rays (b) and natural light (a). Chondrules are marked with the yellow circles, CAIs with the green, and metals with the blue. Larger images can be seen in appendix A.2.*

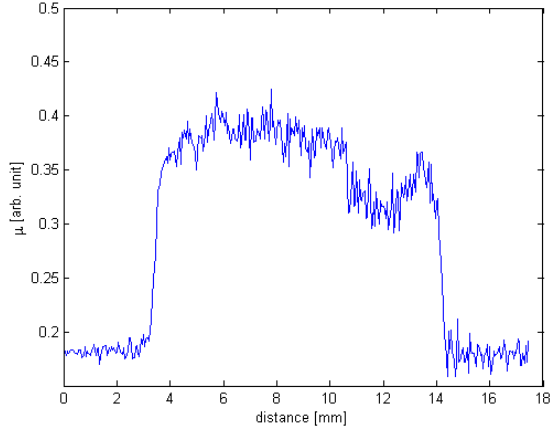
The first thing one notices when comparing the two pictures is that objects clearly distinguishable in one of the images now may not appear as clearly in the other, *e.g.* the object in the upper left corner in figure 22(b) marked with a blue ring is not clearly visible in the photo because of its darker colour.

With the naked eye, chondrules can only be distinguished from CAIs because of the differences in shape. They both appear as darker areas in the X-ray image; therefore they are not distinguishable by the colour itself. Chondrules can be identified by their round shapes, whereas CAIs are the dark, oddly shaped ones.

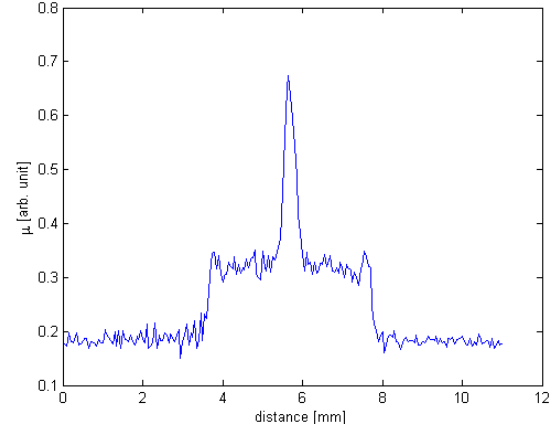
The large CAI that is clearly visible in the middle of figure 22(a) can be identified in the X-ray image, figure 22(b), where it is possible to make out its shape and the small hole in the middle of it. Other CAIs can be identified in similar ways. Several chondrules have been identified in the X-ray image and in the photo.

5.1.2 Profile plots

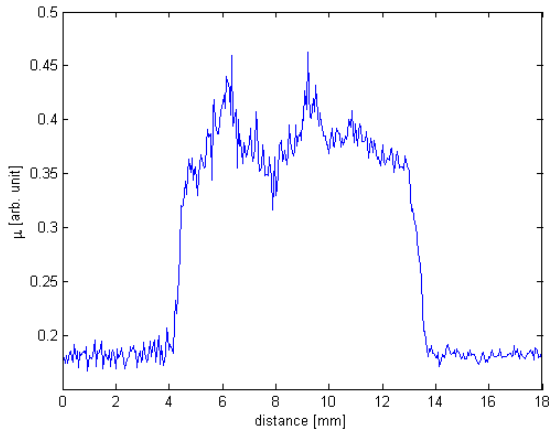
In order to investigate the different attenuation rates of the elements in the stone, we made profile plots using ImageJ. A profile plot shows how the μ -value changes for a line through the meteorite. In



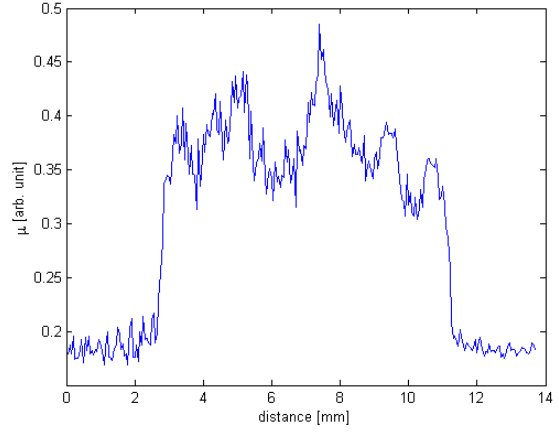
(a) Profile plot through the air, matrix, and a CAI (at 12 mm). The line through the stone can be seen in figure (e).



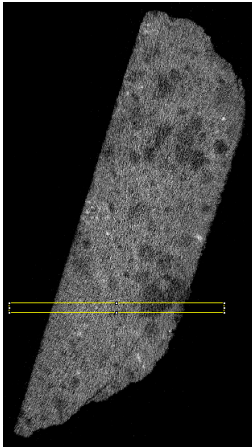
(b) Profile plot through the air and a chondrule with a metal-rich grain in the middle (at 5.5 mm). The line through the stone can be seen in (f).



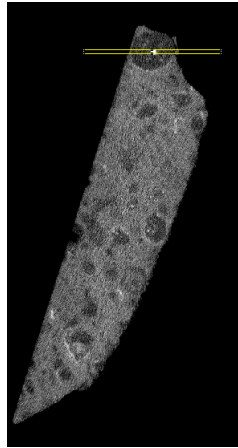
(c) Profile plot through the air, matrix, and Inc1 (at 8 mm). The line through the stone can be seen in (g).



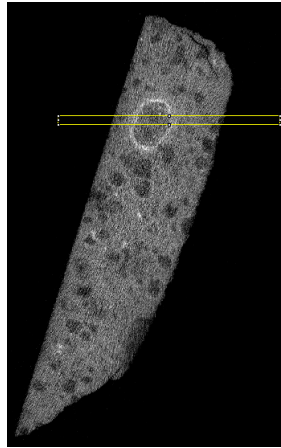
(d) Profile plot through the air, matrix, and Inc2 (at 6.5 mm). The line through the stone can be seen in (h).



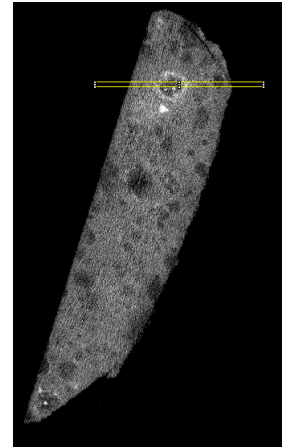
(e) Picture 703



(f) Picture 367



(g) Picture 460



(h) Picture 422

Figure 23: (a) – (c) show profile plots through different parts of the meteorite. (e) – (g) show which part of the meteorite the plots were made from.

order to get a smoother curve, we made quite thick lines (of 10-20 pixels), so each point on the plot is the mean value of all the vertical pixels inside the line. Obviously, one should try to make sure that the values are almost the same perpendicular to the line. Matrix, a chondrule, a CAI, a metal grain, and two white rings are included in the four profile plots shown in figure 23.

From the profiles in figure 23 we can therefore see the μ -values for several of the elements in the stone as well as their approximate horizontal placement. The air surrounding the stone has a μ -value of approximately 0.18 and matrix has one of about 0.38, which can be seen in *e.g.* figure 23(a).

Figure 23(a) shows a profile plot through a part of the matrix and a CAI; the CAI starts about 3.5 mm into the stone. It has a lower μ -values than matrix of about 0.31. Comparing plot 23(a) and (b), you cannot see any clear difference between the value of the CAI and the Chondrule – their attenuation are similar. The only way to distinguish between them in tomographic images is again their shape, not their attenuation.

About 2 mm into the chondrule in figure 23(b),(f) there is a small, round, white inclusion with a very high attenuation coefficient of about 0.67. This is probably a metal-rich grain, which may be comprised of troilite, FeS.

We also made a profile plot through a chondrule with white droplets around the edges. This plot can be seen in appendix A.3. The white droplets had a high attenuation coefficient of about 0.5.

The plots of the two white rings are a bit more crowded. Figure 23(c) shows a profile plot through the inclusion we had previously seen on the neutron tomographic image (from here on denoted Inc1); the two edges of the inclusion are at about 6 and 9 mm on the graph, respectively. The edge's absorption coefficient is about 0.45, so it is a bit higher than that of the matrix, but nowhere near as high as what we determined to be a metal grain in figure 23(b). However, the edge clearly consists of some sort of heavy mineral.

An inclusion that did not show up on the old neutron tomographic image, but is situated right next to Inc2, is shown in figure 23(d). This inclusion will be called Inc2 in the following. The inclusion's edges are at about 5 and 7.5 mm on the graph, respectively, with μ -values of roughly 0.45.

We also made a profile plot through the double white rings (Inc3), seen at the bottom of figure 18(b). The plot can be seen in appendix A.4. The white rings have values of about 0.46.

Inside all the inclusions, μ is lower than the matrix value. All the white rings are probably rims around chondrules.

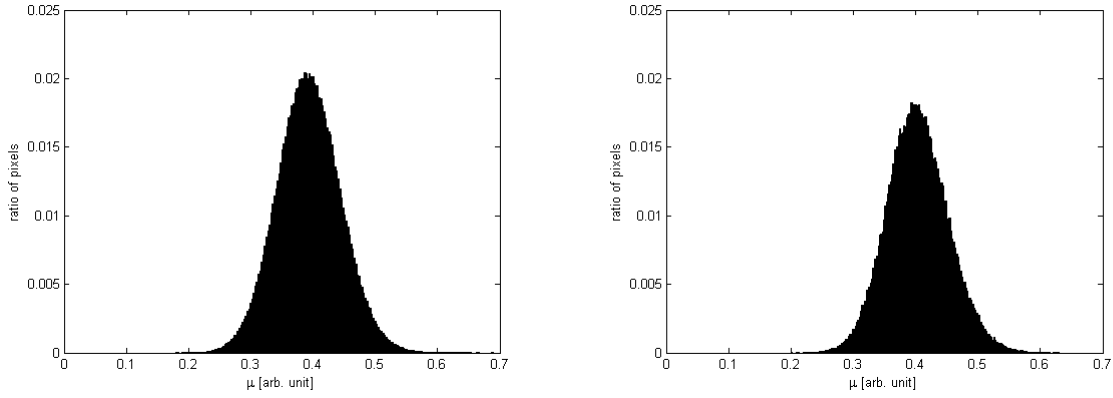
It is important to note that all the inclusions' edges does not have uniform values at all. Depending on where the profile plot was made, the μ -value of the rings could be as high as 0.56. Therefore, in order to investigate the voxel values further, histograms are made for volumes around Inc1 and Inc2.

5.1.3 Histograms

In order to further investigate specific sections of the stone, we made normalized 3D histograms of the inclusions. The histograms shows the ratio of voxels in the entire sample with specific μ -values and were made using a NumPy program provided by Brian Vinter at eScience, NBI, which gave a string of data plotted using Matlab version 2011a. Two histograms are shown in figure 24, for volumes around Inc1 and Inc2.

Figure 24(a) shows a histogram for a volume around Inc1. Most of the voxels have μ -values around 0.4 – this is the matrix around the inclusion – but there are also voxel values as low as 0.18 and as high as 0.7. The values above 0.45 are the ones belonging to either the white circle, or the little white dots inside it; this can be gathered from the profile plots in the previous section. A small ratio of the voxels have μ -values lower than 0.3, *i.e.* lower than that of chondrules and CAIs and therefore may be from less dense elements or voids.

Figure 24(b) shows a histogram for an area around Inc2. This histogram is very similar to that in 24(a); the largest ratio of voxels are again around 0.4, and the maximum and minimum values



(a) Histogram of a volume around Inc1, using the coordinates $x=(264;347)$, $y=(229;325)$, and $z=(427;496)$ in Python. Thus it has values from ~ 550000 voxels. (b) Histogram of a volume around Inc2, using the coordinates $x=(294;364)$, $y=(199;256)$, and $z=(399;447)$ in Python. Thus it has values from ~ 190000 voxels.

Figure 24: *Histograms around the Inc1 and Inc2, both using 200 bins.*

are approximately that of the Inc1. For X-ray tomography in this resolution, there really is not any significant difference in attenuation between the two inclusions.

A table of the approximate values of μ for the different elements, as estimated from the profile plots and histograms, can be seen in table 3.

Component	$\sim \mu$ [arb. unit]
Air	0.18
Matrix	0.38-0.42
Chondrules, interior	0.30-0.35
Metal-rich grain	0.67
Inc1, rim	0.45-0.56
Inc2, rim	0.45-0.56
Inc3, rims	0.45-0.48
droplet rim	0.5
Whole stone	0.4

Table 3: *A table of approximate μ -values for several of the elements in Allende*

The scale of the X-ray pictures is, besides being in arbitrary units, somewhat strange: the air does not have values near zero. The attenuation of air is next to nothing, and its value *should* be zero. The value of air is not due to the polystyrene, as this only covered half of the sample, and the air has similar values everywhere.

5.2 Neutron Tomography

5.2.1 Discussion

In the reconstructed tomographic images from the new neutron data, one of which can be seen in figure 20, several more components can be distinguished than in the old neutron pictures, see appendix A.1. The chondrules and CAIs can clearly be distinguished from the brighter matrix material.

The chondrules next to Inc1, whose rim we saw in the X-ray images, can also be discerned on the neutron images. However, they do not appear as bright as Inc1's edge. Several metal grains also appear clearly; all these elements can be seen in figures 26(e)–(h).

5.2.2 Comparison of stone and neutron

Once again, we made a tomographic image right beneath the surface with Slicer and compared it with the photo of the stone; the comparison is shown in figure 25, and larger images can be seen in appendix A.5.

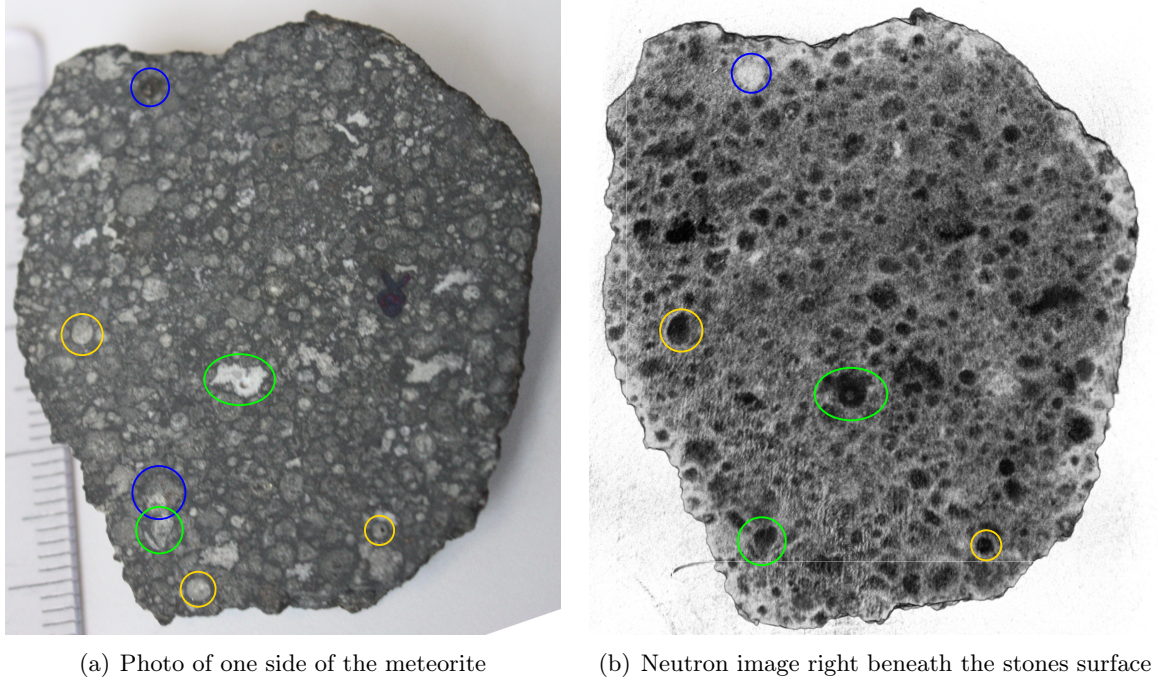


Figure 25: *The surface of the stone as seen by neutrons (b) and natural light (a). Chondrules are marked with the yellow circles, CAIs with the green, and metals with the blue. Larger images can be seen in appendix A.5.*

Like on the X-ray images, several components are distinguishable on the neutron images. The metal in the top-left corner is white as expected, being highly attenuating, and the CAI with the hole in the middle is also visible, as well as several chondrules and other CAIs.

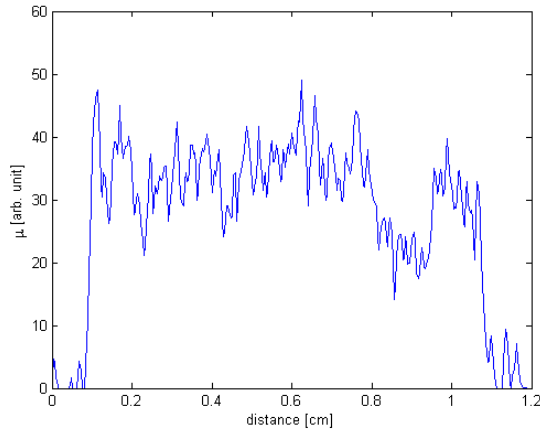
5.2.3 Profile plots

Profile plots were made through the same kind of components as we did for X-ray using ImageJ. They can be seen in figure 26. From these plots we can once again see the attenuation coefficients of several elements in the stone as well as their approximate horizontal placement. The air surrounding the stone has a μ -value of approximately 0 and the matrix has one between 40 and 55. The variation in attenuation coefficient is due to the fusion crust which appears brighter as seen in *e.g.* figure 27, this alteration is probable due to the meteors passing through the atmosphere.

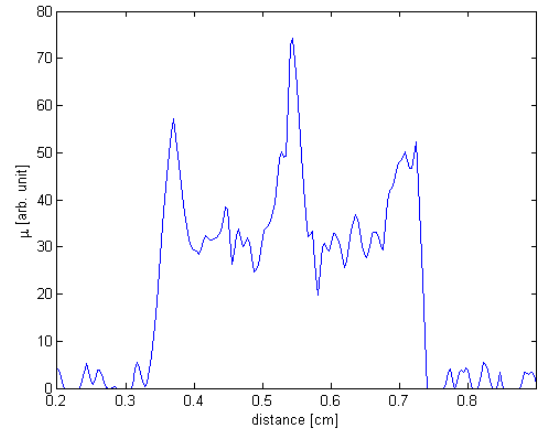
Figure 26(a) shows a profile through the air, matrix, and a CAI. Like in the X-ray data, the CAI has a lower attenuation than the surrounding matrix, of about 30. This is quite a bit lower than the chondrule in 26(b), which have a value of about 20, but other chondrules have values as low as the CAI. Therefore chondrules and CAIs can again only be distinguished by their shape in neutron tomography.

About 2 mm into the chondrule in 26(b),(f) there is a grain with an attenuation coefficient of about 72. This suggests, like the X-ray data, that the grain probably consists of some kind of metal-rich mineral.

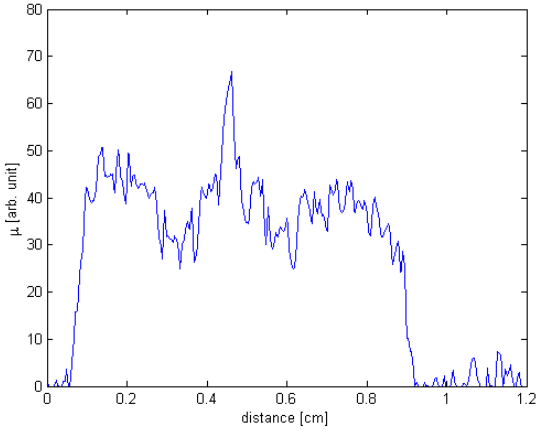
Figure 26(c) shows a profile through what you can see of Inc2. It has a value of about 65, *i.e.* lower than the value of the metal-rich grain in figure 26(b), so it is definitely not hydrogen.



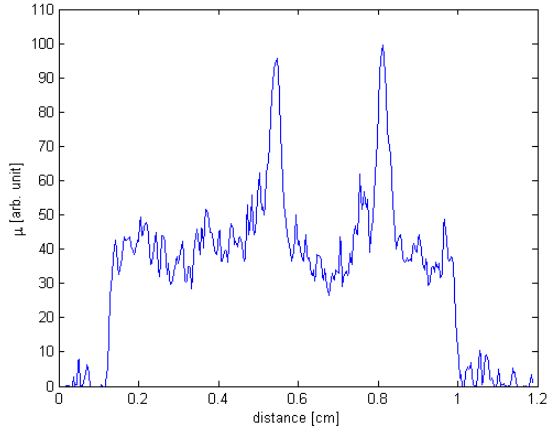
(a) Profile plot through the air, matrix, and a CAI. The line through the stone can be seen in figure (e).



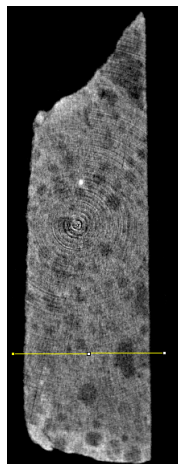
(b) Profile plot through the air and a chondrule with a metal grain in the middle. The line through the stone can be seen in (f).



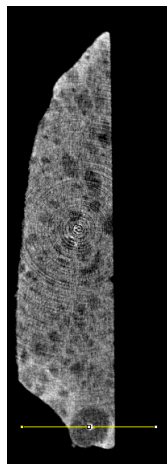
(c) Profile plot through the air, matrix, and Inc2. The line through the stone can be seen in (g).



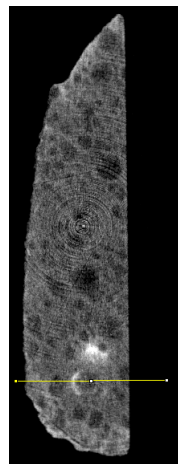
(d) Profile plot through the air, matrix, and Inc1. The line through the stone can be seen in (h).



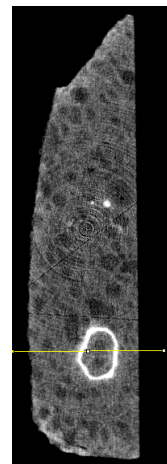
(e) Picture 879



(f) Picture 519



(g) Picture 627



(h) Picture 679

Figure 26: (a)–(d) show profile plots through different parts of the meteorite using neutron images. (e)–(h) show the corresponding line through the meteorite.

Inc1 has a very high X-ray attenuation, of about 100, see figure 26(d). This is at first glance too high to be a metal rim on a chondrule, and it more likely consists of some kind of hydrogen mineral. We will try to further investigate this inclusion in the following sections. Inside the inclusion, its value is approximately that of a chondrule.

5.2.4 Histogram

In order to further investigate Inc1, we made a normalized histogram over one slice including Inc1 as seen in figure 27. As the NumPy program we used to make histograms over volumes of the X-ray data only accepts .raw-files, and we only had Tiff-picture of the neutron data, the histogram was made using ImageJ.

In the histogram you can see that the attenuation coefficients have a large range, with a peak value around 40 – this is the matrix-material and the inner parts of the inclusion. The μ -values above 75 are the ones belonging to the rim of the inclusion.

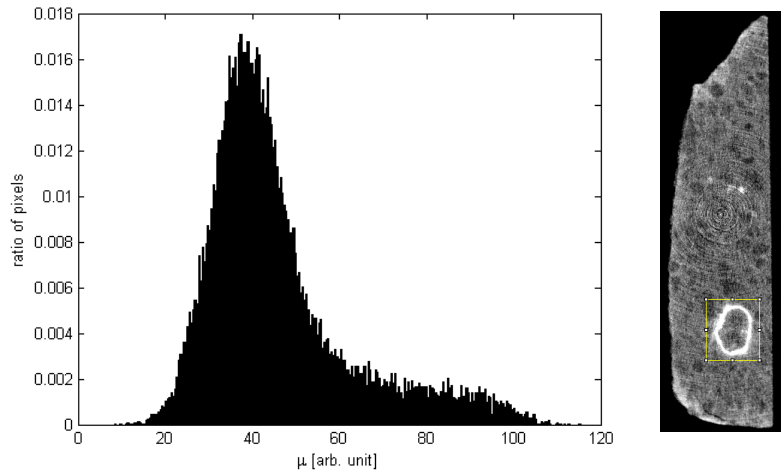


Figure 27: *Normalized histogram of the white inclusion and the area over which it was taken on picture 684.*

A table of the approximate values of μ for the different components, as estimated from the profile plots and the histogram, can be seen in table 4.

Component	$\sim \mu$ [arb. unit]
Air	0
Matrix	40-50
Chondrules, interior	20-30
Inc1, rim	75-115
Inc2, rim	65
Metal-rich grain	72
Whole stone	35

Table 4: *Approximate neutron μ -values for several components in Allende.*

As opposed to the greyscale of X-ray, air *do* have a value of zero in the neutron greyscale, as we would expect.

5.3 Investigation of the inclusion

The inclusion previously found on neutron, Inc1, can also be seen in the X-ray images. The first thing one notices about it, is that it is not perfectly round, but has an oval shape with an indent, as can be seen in figure 1 and 28. This, however, is not abnormal for chondrules as they are not always spherical; they could *e.g.* have been dented by an impact with another chondrule while it was still warm enough to be plastic. Thus, Inc1 is probably a normal chondrule with an abnormal rim.

Both X-ray and neutron images show multiple high-attenuating rims. Normally the rim, consisting of varying kinds of minerals, would appear as spaced droplets as opposed to the continuous rim present on several of our chondrules, including Inc1. The continuous rims are consistent with what J.M. Friedrich [22] observed, as shown on figure 9. It could be the result of a melting of what once was droplets.

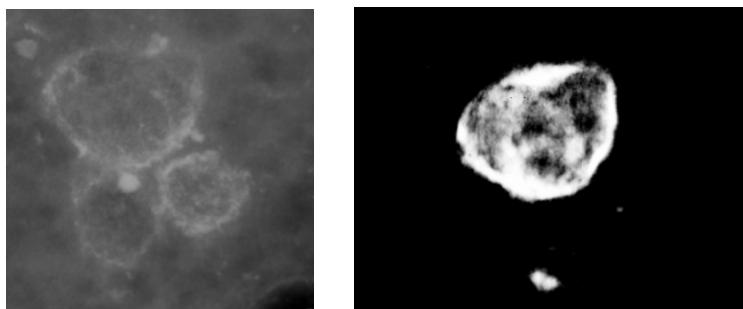


Figure 28: 3D tomographic X-ray and neutron images of the inclusion Inc1 made in Slicer, with the air and most of the matrix removed.

If the inclusion was dark on X-ray, the rim of the inclusion could probably be determined to be rich in hydrogen, which is low attenuating of X-rays, but has a high neutron attenuation coefficient.

The metal grain and the rims of the chondrules have an experimental attenuation coefficient almost double that of the whole stone. If the background attenuation is as calculated, 45 m^{-1} , only pure nickel, which does not exist in chondrites, would justify this. The abundance of hydrogen in our piece of Allende thus has to be lower than the standard value in CV-chondrites, lowering the overall background.

It is not implausible that our stone has a much lower mean attenuation, as small differences in hydrogen abundance affects the value drastically.

Since we do not know the value of the whole stone in cm^{-1} , we cannot from the neutron images alone refute that the attenuation of Inc1's edge is due to it being more rich in nickel or iron than the other rims. This, however, does not seem likely when comparing with the X-ray attenuations, as it would not explain why the attenuation rates in the X-ray images are the same for Inc1 and Inc2-3, but differ quite a bit in the neutron images. If the higher neutron attenuation of Inc1's edge is due to a higher concentration of metal, it would have a higher attenuation in the X-ray images as well. This suggests that the edge consists of hydrogen mineral, as well as metal; hydrogen has a very high neutron attenuation coefficient, so even a small amount would change the attenuation of neutrons significantly inside the voxels, but would barely lower the X-ray attenuation.

In theory, the high attenuation could also be caused by another high-attenuating element, like *e.g.* chlorine, but it exists in so small quantities in CV-chondrites that this is highly unlikely. Therefore, the most likely explanation is that Inc1's edge consists of some sort of hydrogen-containing mineral.

This inclusion will certainly require further investigation into its composition.

A way hydrogen could be present is by hydrazation, meaning it 'hides' inside the empty space inside the crystal lattice of metal, which would explain why the rim lights up on both X-ray and neutron. This preferential concentration of hydrogen is unlikely, as the chondrules have been heated after accretion;

even a heating to a couple of hundred degrees would make the hydrogen diffuse to the other chondrule rims as well. The explanation probably is that the rim consists of some kind of hydrogen mineral; if the hydrogen is bound in a mineral, it cannot escape during heating.

The chondrule probably came in contact with some ice which then melted, introducing the hydrogen to the rim. This means that this chondrule probably has travelled a different way through the nebula than the other chondrules in our piece.

The rim could actually also be two concentric rims, one of metal-minerals and the other of volatile minerals containing hydrogen.

6 Further research

The obvious first step for further investigation of our piece of Allende would be to conduct a new X-ray experiment, in order to determine the attenuation coefficient in 'proper' units.

If this is done on the same machine – the Nanotom – we would have to run a reference sample with a known μ -value. Thus the data output of the reference material can be compared with the known μ -value, and this will allow us to determine the attenuation coefficients in the stone. However, the images of the stone and the reference have to be taken simultaneously, otherwise the comparison cannot be done. This is a flaw when using the software on this machine.

Another opportunity is to use a different machine, *e.g.* the X-ray facilities in Munich or PSI, where transmission images are part of the output. At PSI, neutron and X-ray imaging can in addition be done with almost identical recording geometries – that way a comparison of the two is easier.

To examine the stone in better resolution via X-rays, it would have to be chopped into smaller pieces. Ebel and Rivers showed that with sample sizes of 0.5-3.0 cm³ and a resolution at 10-17 μ m [6], chondrules and CAIs were even more clearly distinguishable from matrix and could be analyzed individually.

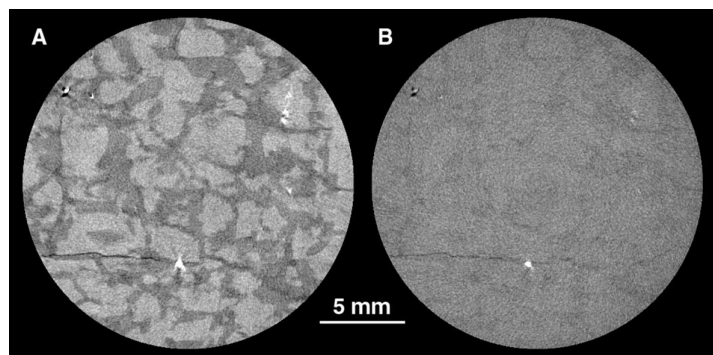


Figure 29: *Tomographic images of a drill-core of granite at low and high energies. A is for 100 keV and B is for 200 keV [19].*

If one wanted to discern between components of minerals with similar attenuation coefficient in our X-ray image, you could perform another experiment but at a lower effective energy, making the absorption of photons the primary reason for attenuation instead, as described in section 2.2.4, thus enhancing the differences between the components of interest.

This is illustrated in figure 29, where a core of granite is probed at 100 keV and 200 keV, clearly showing that contours of two minerals in granite, quartz and orthoclase, that are not easily distinguishable at high energies can be visible at lower energies. The two minerals had identical attenuation coefficients at 125 keV, but appear as two distinct components at 100 keV; this can be seen in figure 7.

However, at low energies, the transmission of the beam gets smaller, and as calculated in section

3.2.1 below an effective energy of 100 keV, tomography would not be possible for our sample. So in order to be able to utilize the absorptions' dependency on energy, our sample would have to be sliced into a smaller piece that are penetrable to a beam of lower energy.

In section 5.1.1 we compared the surface of the stone in natural light with an X-ray tomographic image. We only described what we could see with the naked eye, but if we had used a microscope, we would have been able to identify aggregates of individual minerals.

This, apart from being informative about the mineralogy and composition of the meteorite in itself, could be used as a reference for a conversion between the greyscale voxel values and physical attenuation coefficients. One such mineral could be olivine, $(\text{Mg,Fe})_2\text{SiO}_4$, that can be distinguished by its greenish colour. This would of course require an amount of the mineral great enough to be seen at the resolution of the tomographic image; *i.e.* the amount is great enough to justify a voxel of its own.

However, as mentioned above, in order for the difference between olivine and a similar mineral not to be extinguished, making it harder to pinpoint its location on a X-ray image, the energy would have to be low enough – this in return requires a sample thin enough, so that transmission is possible.

To be able to distinguish between different metals, another non-destructive investigation method can be used. Wavelength resolved neutron tomography at *e.g.* PSI, can be performed in order to determine the spacing between the planes in the atomic lattice d using Bragg's law *i.e.* $n\lambda = 2d\sin(\theta)$. By changing the wavelengths you can find the position of the Bragg edge. The edge results from coherent scattering on the crystal planes, because a given plane can only reflect wavelengths shorter than $2d$. The Bragg edge corresponds to $\theta = 90^\circ$, *i.e.* when $n\lambda = 2d$, and from this the lattice constant d can be found.

One interesting aspect of the stone, besides Inc1, that could compel further investigation is the large chondrule that we used to make the profile plots in figure 23(b) and 26(b). The chondrule is clearly visible in both X-ray and neutron images, where several high attenuating grains can be seen. It is this amount of grains that distinguishes it from the other chondrules and makes it an area for further studies.

7 Conclusion

The purpose of this thesis was to investigate the internals of the Allende meteorite using non-destructive methods. The meteorite had previously been examined by neutron tomography in 2005 and an interesting inclusion was found; by doing another neutron experiment with better resolution in addition to X-ray tomography, we wished to investigate the composition of this inclusion. In addition, we hoped to see other interesting elements in the stone.

It has been shown that a tomographic scan of our entire piece of Allende is possible with both neutron and X-ray tomography, despite the large abundance of iron. The X-ray experiment was done on the phoenix Nanotom at Novo Nordisk in Hillerød, and both neutron experiments were done on the NEUTRA beamline at PSI in Switzerland. In the end we had new tomographic images with a resolution of 25 μm for X-ray and 31.6 μm for the new neutron data.

However, as we were investigating a stone which is quite heterogeneous, the X-ray images were very grainy in full resolution. Therefore we decided to process the data in half resolution, 50 μm . If you want to investigate the stone with X-rays in better resolution, you would probably need to look at smaller pieces. In addition, if the experiment is conducted at lower energies, it will be easier to distinguish between the different minerals.

In the X-ray and neutron images you can clearly see both CAIs, chondrules, metal minerals, and the inclusion previously seen on the old neutron images (called Inc1). In addition, several high attenuating rims around chondrules can clearly be distinguished in the X-ray pictures. All the high attenuating

rings, including the edge of Inc1, are probably rims on chondrules.

By making profile plots and histograms over several areas of the tomographic images, we were able to approximate values for the attenuation coefficient of several elements in the stone. The attenuation coefficients were approximated for the air, matrix, chondrules, a metal mineral, and the inclusion for both neutron and X-ray tomography, as well as the X-ray attenuation of the several rims on chondrules. The values can be seen in table 3 for the X-ray images, and in tabel 4 for the neutron images.

Unfortunately, the μ -values from X-ray are not in m^{-1} , as the Nanotom measured the values in some arbitrary unit which cannot be converted. In addition, the neutron data are also in arbitrary units, as the unit was not taken into consideration during the reconstruction.

One interesting aspect is that Inc1's edge does not seem to differ from the other white inclusions in the X-ray images. Thus it is definitely useful to combine the two techniques, as one can provide valuable information the other does not. From the X-ray images, it looks like the edge consists of the same material as the other rims on chondrules, which most likely consist of some metal-rich element.

From the neutron images alone we cannot dispute the theory that the high neutron attenuation of Inc1's edge is due to nickel or iron. However, when comparing the neutron μ -values with the ones for X-ray, this theory seems highly unlikely; whereas Inc1's edge has the same values as all the other inclusions in the X-ray images, it differs quite a bit from them in the neutron images. If Inc1's edge consisted of more metal than the other rims, its attenuation would be higher in the X-ray images. In addition, its neutron attenuation is even higher than the presumed metal-rich grain, which was more high-attenuating in the X-ray images, making its values stand out even more. Therefore it is more likely that the edge consists of hydrogen and metal; small changes in hydrogen abundance would change the neutron attenuation significantly, but would not change the X-ray attenuation much.

The attenuation of Inc1's edge could also be due to another element where small quantities give a very high neutron attenuation *e.g.* chlorine; however, since they only exist in very small quantities in CV-chondrites, the most plausible explanation is that the high attenuation is because of hydrogen.

The presence of chondrules with rims in the vicinity of Inc1 makes deposition of hydrogen in the crystal lattice an unlikely senario as post-accretion heating makes preferential concentration implausible. Therefore the incorporation of hydrogen in the edge must have happened pre-accretion as a constituent of a mineral. The chondrule probably travelled a different path through the nebula than the other chondrules where it came in contact with some ice; when the ice melted, the hydrogen was introduced to the minerals of the rim.

Another explanation for the inclusion appearing in both X-ray and neutron images is that the edge of Inc1 and the other rims are made from the same X-ray high-attenuation element, *i.e.* a metal-rich mineral, and that the inclusion in addition has a rim made up of more volatile minerals containing the neutron high-attenuation hydrogen.

An answer to the above mentioned questions will require further research and experimental investigation beyond the scope of this project and possibly also beyond the abilities of non-destructive techniques. However, like *e.g.* Denton Ebel found [6], we have illustrated that the method of tomography is helpful in illuminating and determining areas of interest, thus being the obvious first step when investigating the interior of rare meteorites, before more invasive procedures are evoked.

References

- [1] W.J. Borucki et al, “Characteristics of planetary candidates observed by Kepler. II. Analysis of the first four months of data,” The Astrophysical Journal, vol. 736, no. 19, 2011.
- [2] H. Rollins, Early Earth Systems - A Geochemical Approach. Blackwell Publishing, 2007.
- [3] P. A. Bland, A. D. Rothery, N. McBride, I. Gilmour, E. A. Moore, and M. Widdowson, An Introduction to the Solar System, ch. 9. Cambridge University Press, 2011.
- [4] L. S. Schmidt, S. S. Duchnik, M. Lanzky, and M. M. Pedersen, “Mossbauer-spektroskopi af Maribometeoritten.” University of Copenhagen, June 2011.
- [5] W.J. Borucki et al, “Determination of the petrologic type of CV3 chondrites by Raman spectroscopy of included organic matter,” Geochimica et Cosmochimica Acta, vol. 70, no. 7, 2006.
- [6] D. S. Ebel and M. L. Rivers, “Meteorite 3-D synchrotron microtomography: Methods and applications,” Meteoritics & Planetary Science, vol. 42, no. 9, 2007.
- [7] B. Schmitz and M. Tassinari and B. Pecker-Ehrenbrink, “A rain of ordinary chondritic meteorites in the early Ordovician,” Earth & Planetary Science Letters, vol. 194, no. 1-2, pp. 1–15, 2001.
- [8] G. R. Huss, A. E. Rubin, and J. N. Grossman, “Thermal Metamorphism in Chondrites,” in Meteorites And the Early Solar System II (H. Y. McSween, H. Y. M. Jr., and R. P. Binzel, eds.), ch. 7, pp. 567–586, University of Arizona Press, 2006.
- [9] E. R. D. Scott, “Chondrites and the Protoplanetary Disk,” Annual Review of Earth and Planetary Sciences, vol. 35, pp. 577–620, 2007.
- [10] Marmet Meteorites homepage, “<http://www.marmet-meteorites.com/id46.html>.” (07.04.2012).
- [11] K. K. Larsen, A. Trinquier, C. Paton, M. Schiller, D. Wielandt, M. A. Ivanova, J. N. Connelly, A. Nordlund, A. N. Krot, and M. Bizzarro, “Evidence for magnesium isotope heterogeneity in the solar protoplanetary disk,” The Astrophysical Journal Letters, vol. 735, no. 2, 2011.
- [12] A. J. Brearly, “Origin of Graphitic Carbon and Pentlandite in Matrix Olivines in the Allende Meteorite,” Science, vol. 285, no. 5432, 1999.
- [13] A. N. Krot and G. Liboure and C. A. Goodrich and M. I. Petaev, “Silica-rich igneous rims around magnesian chondrules in CR carbonaceous chondrites: Evidence for condensation origin from fractionated nebular gas,” Meteoritics & Planetary Science, vol. 39, no. 12, pp. 193–1955, 2004.
- [14] K. Lodders and B. Fegley, The Planetary Scientist’s Companion, pp. 314–316. Oxford University Press, 1998.
- [15] A. C. Kak and M. Slaney, Principles of Computerized Tomographic Imaging. IEEE PRESS, 1987.
- [16] M. Thomsen, “Inspection of subcutaneous injections by x-ray absorption tomography,” Master’s thesis, University of Copenhagen, 2011.
- [17] J. Als-Nielsen and D. McMorrow, Elements of Modern X-ray Physics, ch. 9. John Wiley & Sons, 2011.
- [18] J. A. Seibert and J. M. Boone, “X-Ray Imaging Physics for Nuclear Medicine Technologists. Part 2: X-Ray Interactions and Image Formation,” Journal of Nuclear Medicine Technology, vol. 33, pp. 3–18, 2005.

- [19] R. A. Ketcham and W. D. Carlson, “Acquisition, optimization and interpretation of X-ray computed tomographic imagery: applications to the geosciences,” *Computers & Geosciences*, vol. 27, pp. 381–400, 2001.
- [20] Georgia State University homepage, “<http://hyperphysics.phy-astr.gsu.edu/hbase/particles/neutrndis.html>.” (26.05.2012).
- [21] K. Lefmann, “Neutron Scattering: Theory, Instrumentation, and Simulation.” University of Copenhagen, November 2011.
- [22] J. M. Friedrich, “Quantitative methods for three-dimensional comparison and petrographic description of chondrites,” *Computers & Geoscience*, vol. 34, pp. 1926–1935, 2008.
- [23] D. T. Britt, D. Yeomans, K. Housen, and G. Consolmagno, “Asteroid Density, Porosity, and Structure,” in *Asteroids III* (W. Bottke, A. Cellino, P. Paolicchi, and R. P. Binzel, eds.), ch. 4.2, pp. 485–500, University of Arizona Press, 2002.
- [24] NIST’s X-ray Attenuation Tables, “<http://physics.nist.gov/PhysRefData/FFast/html/form.html>.” (29.02.2012).
- [25] Specifications for Hamatsu detector, “http://sales.hamamatsu.com/assets/pdf/parts_C/c7942sk-05_kacc1118e08.pdf.” (17.05.2012).
- [26] O. Brunkea, K. Brockdorfb, S. Drewsc, B. Mullerc, T. Donathd, J. Herzend, and F. Beckmannd, “Comparison between X-ray tube based and synchrotron radiation based μ CT,” *Proceedings of SPIE*, vol. 7078, no. 1, 2008.
- [27] phoenix Nanotom, *datos|x acquisition. Operation Manual.*, April 2001.
- [28] NIST neutron cross section home page, “<http://www.ncnr.nist.gov/resources/n-lengths/list.html>.” (07.04.2012).
- [29] S. Janssen, “Neutrons for Research: The Spallation Neutron Source SINQ at the Paul Scherrer Institute,” 2011.
- [30] PSI’s NEUTRA page, “<http://neutra.web.psi.ch/facility/index.html>.” (20.05.2012).

A Appendix

A.1 Old neutron experiment

A.1.1 Experimental setup

The old neutron experiment was performed on NEUTRA as well, but in worse resolution; only $200\text{ }\mu\text{m}$. Unfortunately, since it has been seven years since the experiment was conducted, it was not possible to conjure up the details of the experiment.

From this experiment we got two datafiles; 512 Tiff-pictures with slices from one angle (94.4 MB), and 301 Tiff-pictures with slices in another angle (94.3 MB). A picture of how the stone was placed, made from these slices, can be seen in figure 30.

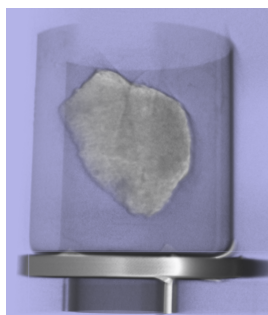


Figure 30: *The placement of the stone in the old neutron experiment, gathered from tomographic images.*

A.1.2 Results

Because we did not have any transmission data of the experiment and the unknown specifics, the unit of the attenuation coefficients remains undetermined.

Two Tiff-pictures of the stone can be seen in figure 31. Figure 31(a) shows the white inclusion and figure 31(c) shows an image with a ring effect, a reconstruction artefact. Both have a colourscale, added in Matlab version 2011a.

Figure 32 shows normalized histograms of the entire sample, made in the open source program ImageJ. As can be seen in 32(a), most of the voxels have an attenuation coefficient of zero; this is because the air around the stone has not been removed from the tomographic image. Therefore, we have zoomed in on the stone's values in figure 32(b). The stone has a mean attenuation coefficient of about 2500 with some voxels lying as high as 5800.

A.1.3 Discussion

As the resolution of the old neutron data is very poor, the only thing that can be clearly distinguished is the strongly absorbing inclusion. Areas of darker colour can be discerned; this is probably the chondrules, but their shape is not clearly defined, except one that can be seen in figure 33(c).

The fusion crust also appears lighter than the rest of the stone as seen in figure 31(c), this is probably due to alterations that occurred during the journey through the atmosphere.

A.1.4 Profile plot

In order to investigate the different attenuation rates of the elements in the stone, we made profile plots through the major components using ImageJ. A profile plot shows how the μ -value changes for a line through the meteorite.

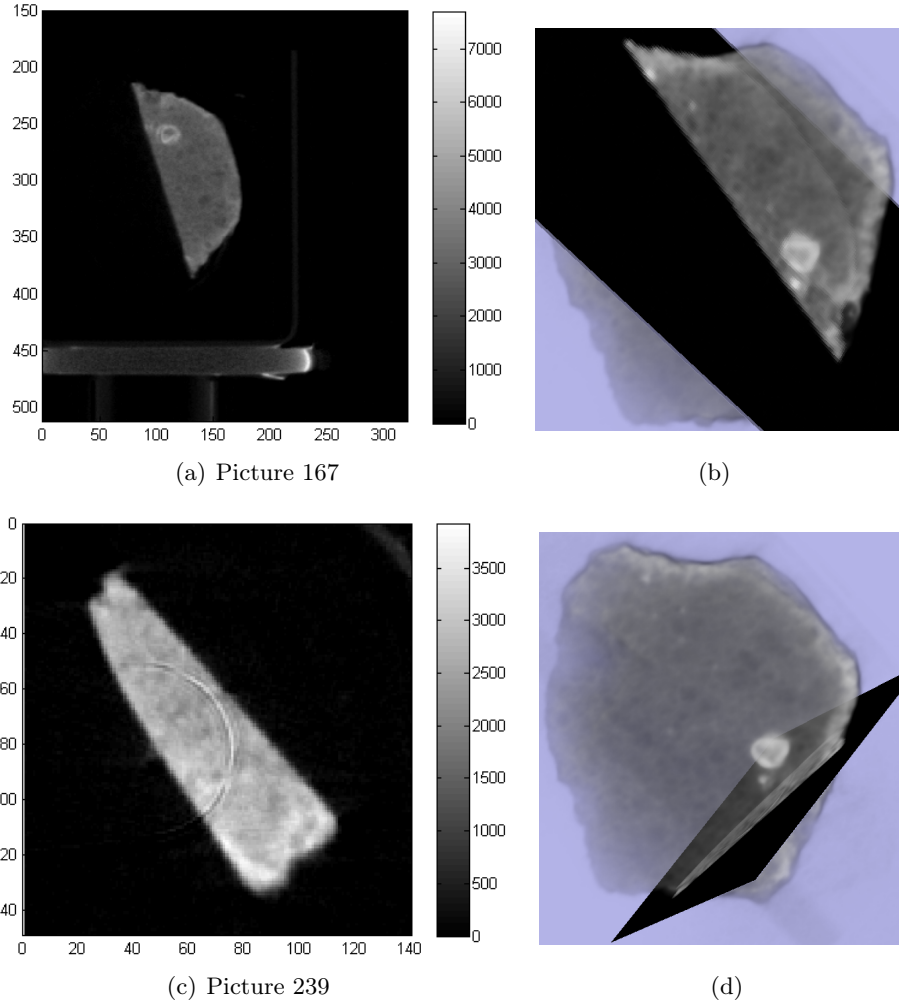


Figure 31: Neutron tomographic slices showing (a) the inclusion and (c) a ring effect. (b) and (d) show the orientation of the slices. The attenuation values are given in some arbitrary unit and the areas with high absorption are white.

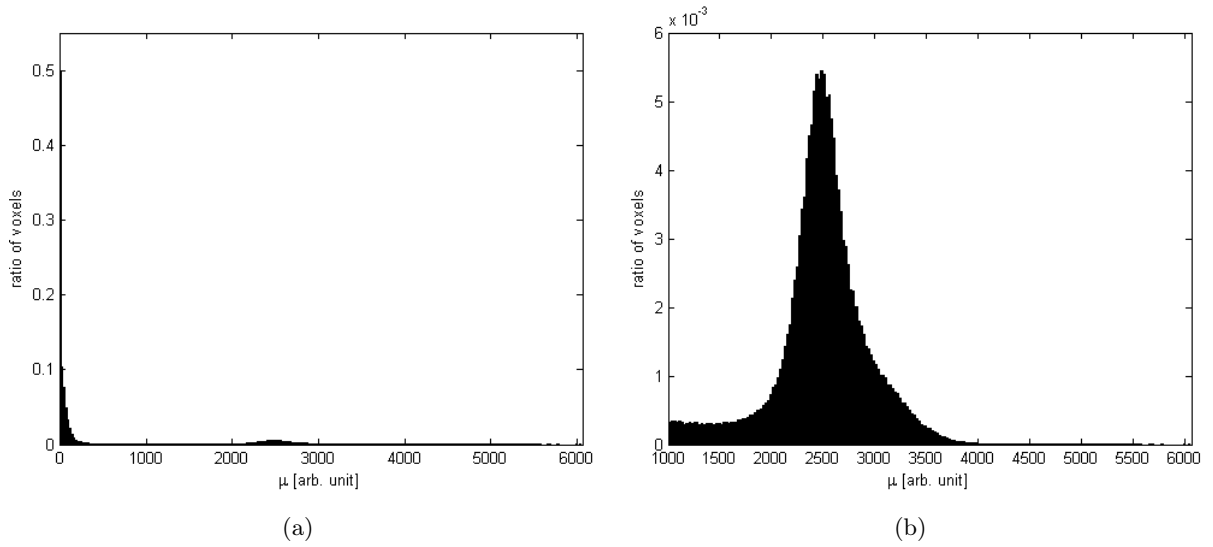


Figure 32: Normalized histograms for the neutron images where (a) shows the whole stone and the air and (b) is zoomed in on the stone's values.

The noticeable things in the low-resolution neutron pictures are the white inclusion and a large chondrule. Their profile plots can be seen in figure 33(a) and (c), respectively.

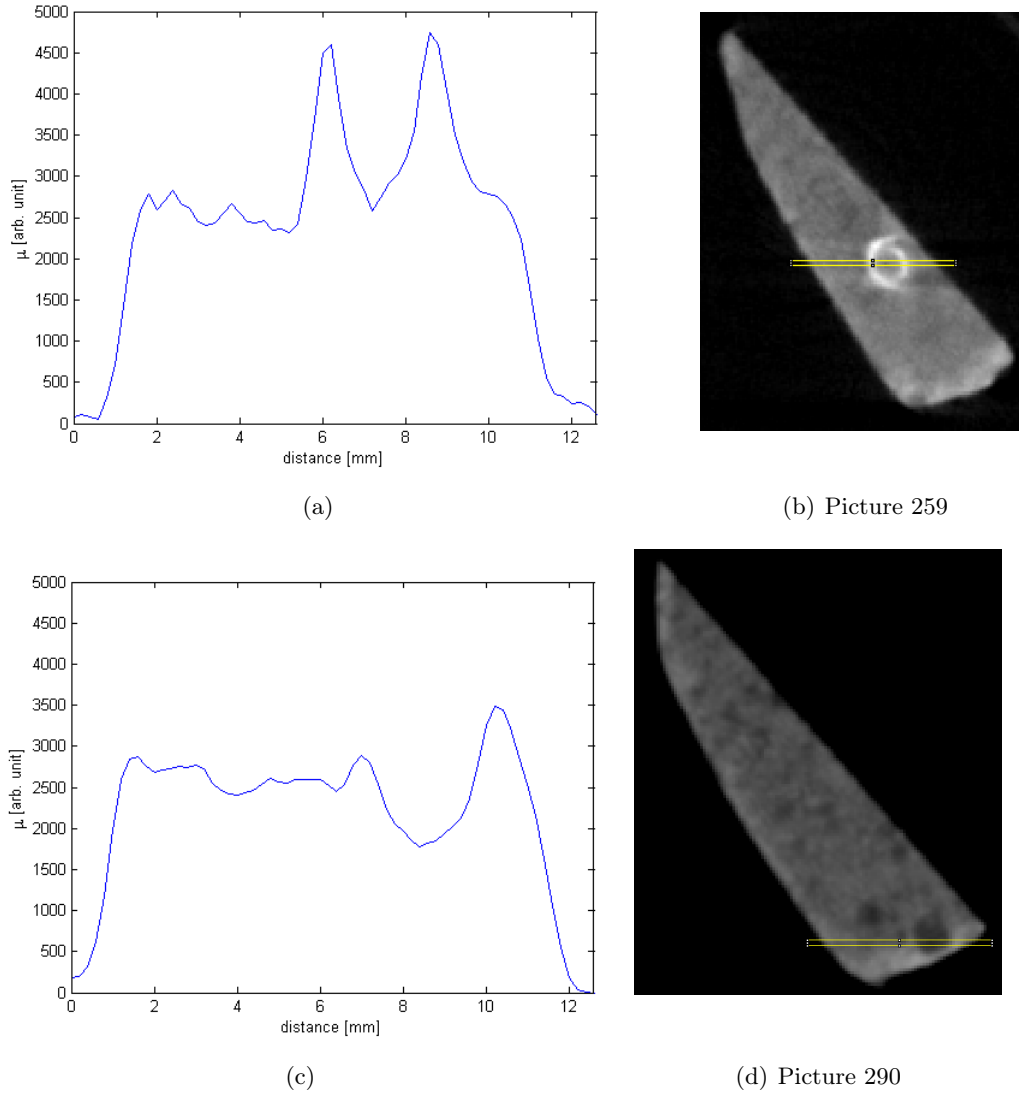


Figure 33: A profile plot through the white inclusion (a) and a chondrule (c) using neutron data. (b) and (d) show which part of the stone the plots were made from.

From the profile plots we can see that the air has an attenuation coefficient of about zero. The white inclusion is clearly visible as the two peaks with μ -values of about 4500. The profile plot through the chondrule can be seen in figure 33(c); the attenuation coefficient is lower than the surrounding matrix with a value of about 1800. In both profile plots we can see that the μ -value of the matrix is about 2700.

A.1.5 Histogram

In order to further investigate the inclusion, we made a normalized histogram over one slice as seen in figure 34. The histogram was made using ImageJ.

In the histogram you can see that the attenuation coefficient have a large range, with a peak value around 2700 – this is most likely matrix and the inner parts of the inclusion. The pixels with μ -values above 4000 are probably the ones belonging to the rim of the inclusion; this could also be gathered from the profile plot.

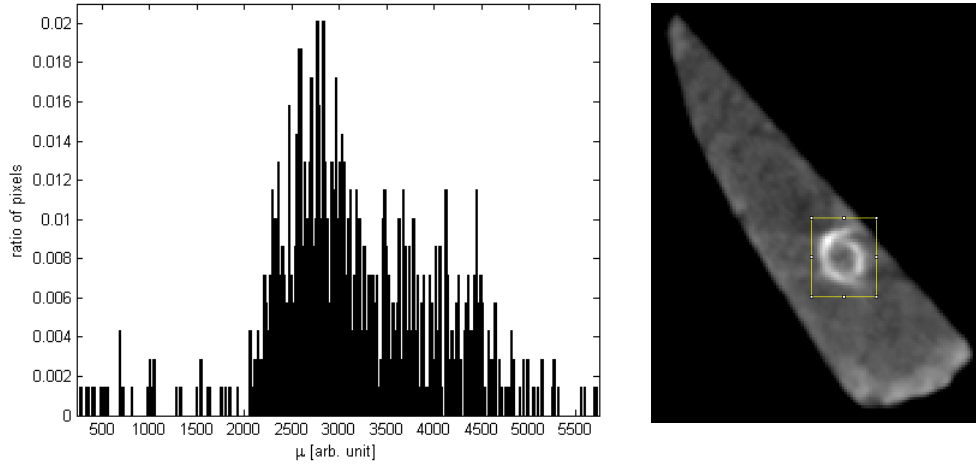


Figure 34: *Normalized histogram of the white inclusion of one slice, picture 258.*

A table of the approximate values of μ for the different elements, as estimated from the profile plots and the histogram, can be seen in table 5.

Component	$\sim\mu$ [arb. unit]
Air	0
Matrix	2700
Chondrules	1800
Inclusion	4000-5700
Whole stone	2500

Table 5: *A table of approximate μ -values for several of the components in Allende for neutron.*

The neutron greyscale values of air is zero, consistent with what we would expect.

A.1.6 Old and new data

The other chondrules' rims do not appear in the old neutron data, but in the new data. This would suggest that the size of the rims of the other chondrules is less than the resolution of the old data; this would make the voxel value a mean of the rim and the surrounding matrix, lowering the value enough to not appear bright on the old neutron data. Inc1 appears in spite of the low resolution due to its content of hydrogen, which is so high attenuating that the matrix does not lower the mean voxel value enough.

At higher resolution, the same rimmed chondrules as on X-ray images appear on neutron images; now the resolution is high enough for the rims' values not to be lowered by the voxel size.

The difference in resolution would also explain why in the old data, Inc1's values is double that of the background of the stone, but in the new data, it is triple; at low resolution more of the Inc1's edges are lowered by surrounding matrix, and at high resolution the edge comprises more voxels and the amount of matrix lowering its value is less.

A.2 Comparison of photo and X-ray

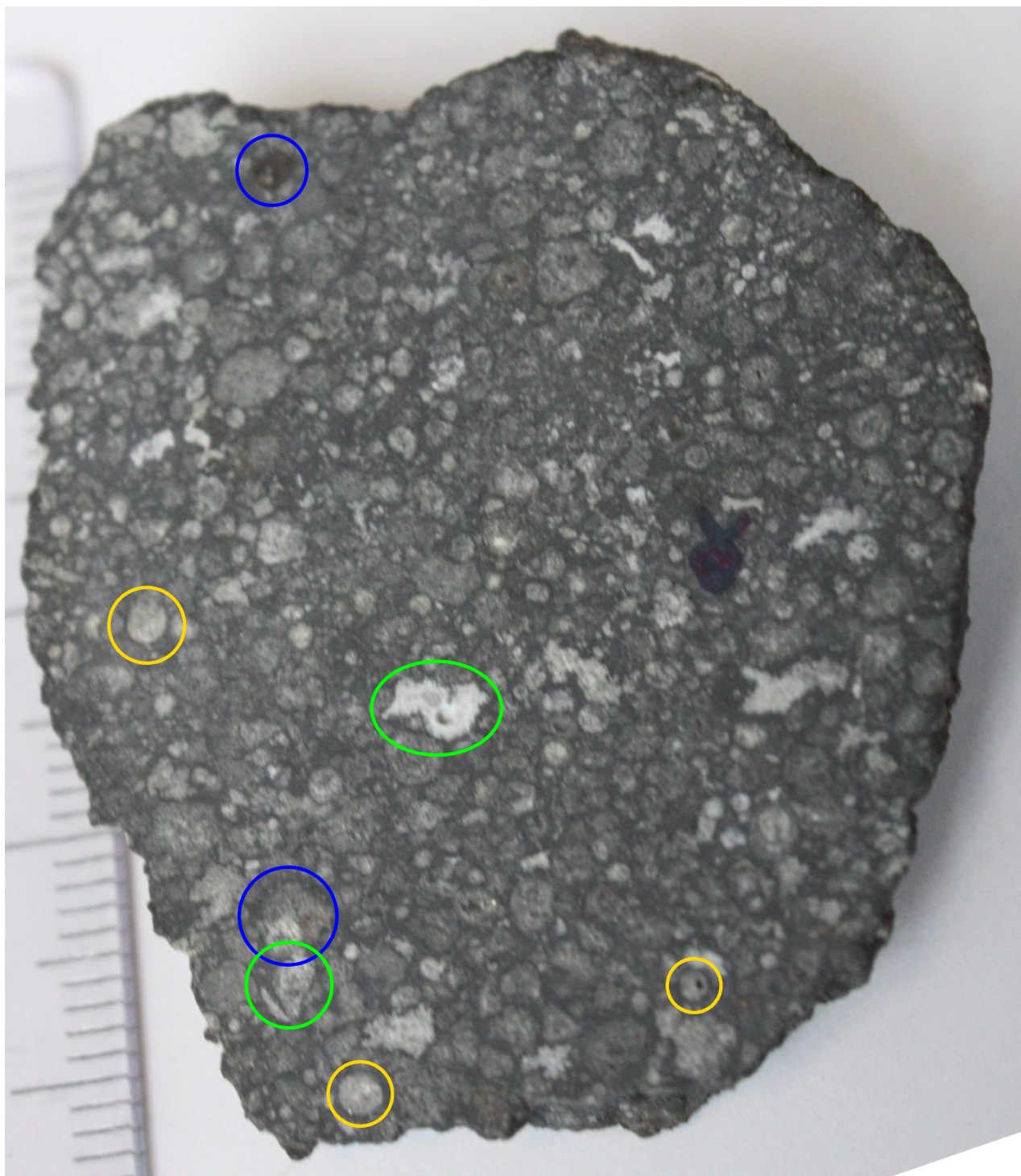


Figure 35: *The surface of the stone as seen in natural light. Enlarged picture of figure 22*

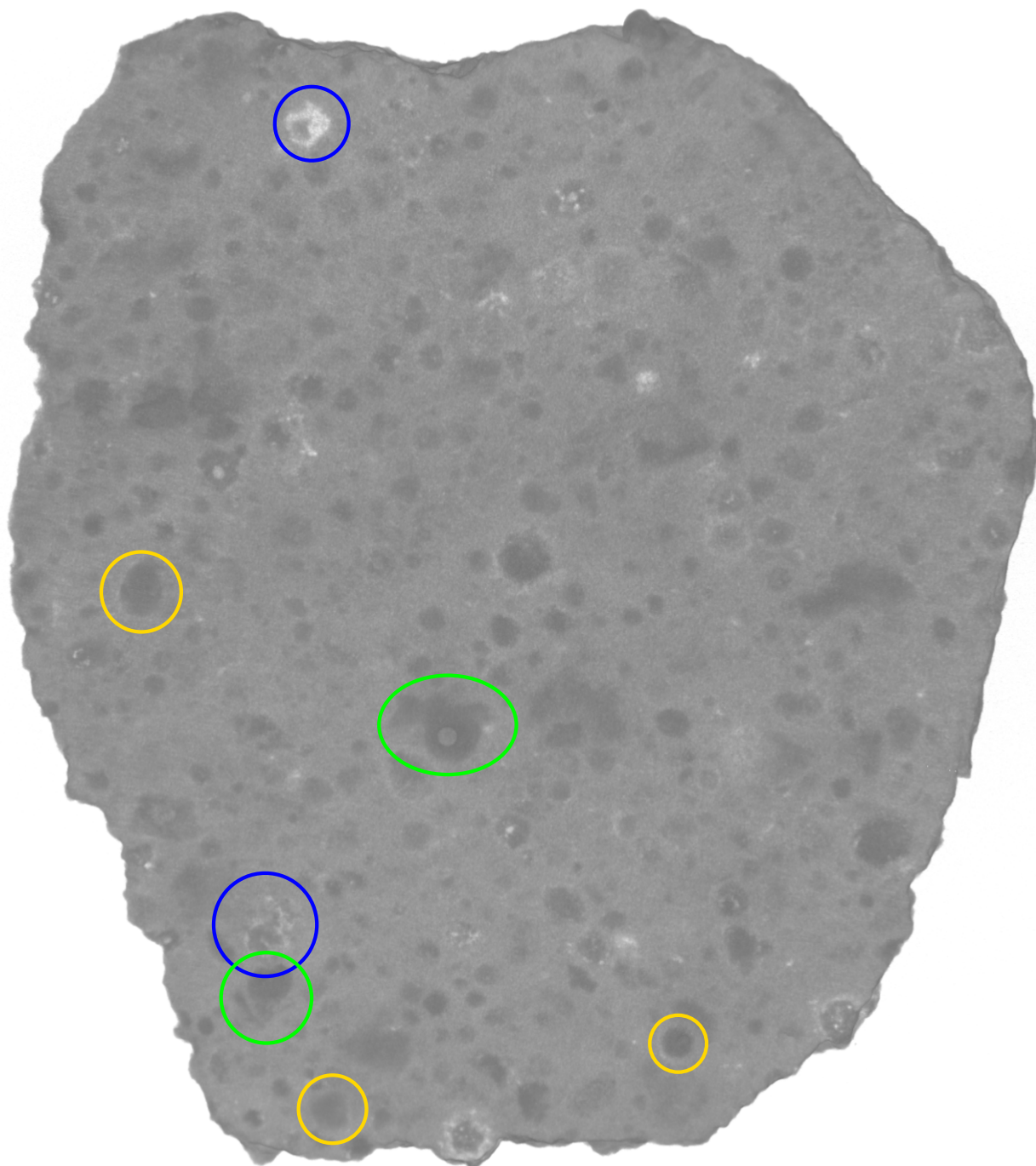


Figure 36: *The surface of the stone as seen by X-rays. Enlarged picture of figure 22*

A.3 X-ray profile plot through droplet

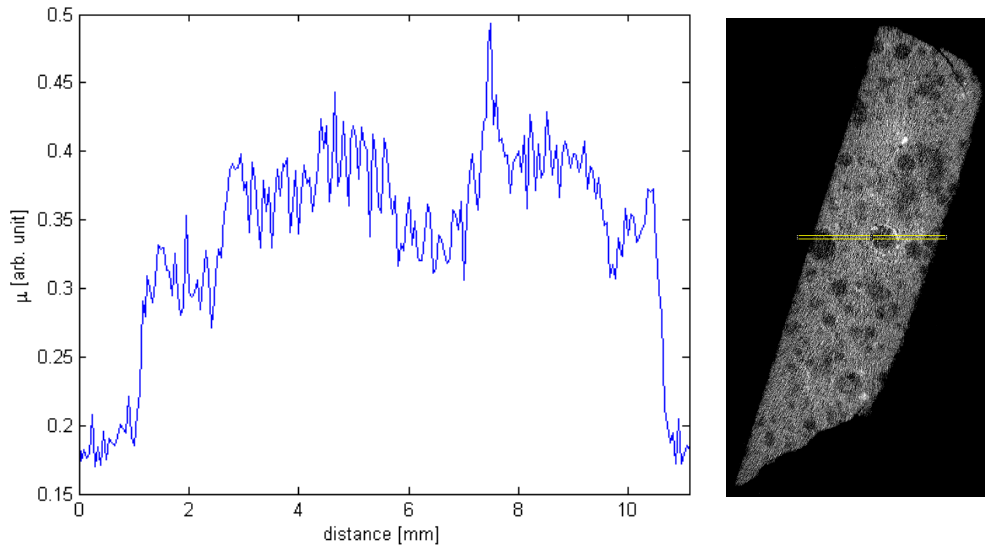


Figure 37: *Profile plot through white droplets on a chondrule's rim, using X-ray data, of slice picture 505.*

A.4 X-ray profile plot through double rims

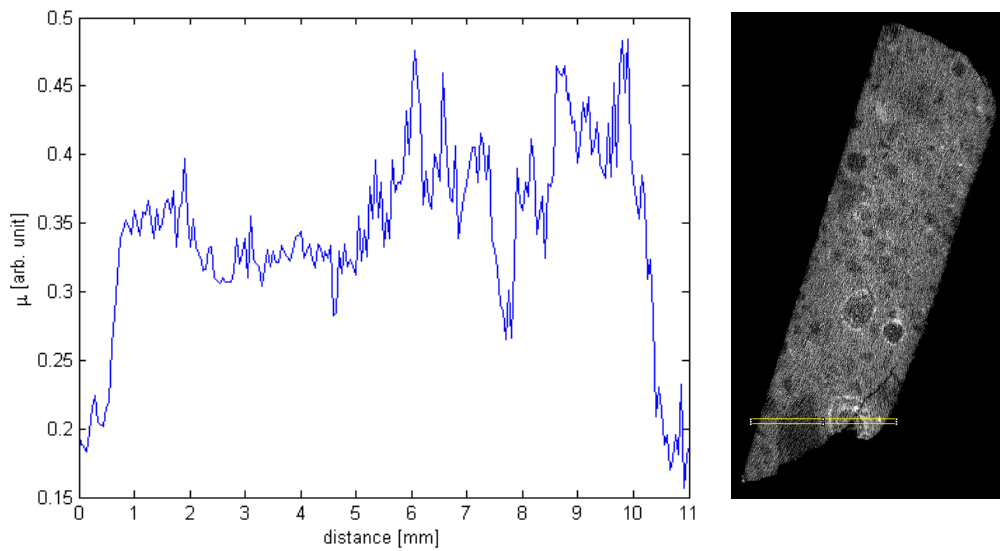


Figure 38: *Profile plot through the double rims using slice picture 638.*

A.5 Comparison of photo and neutron

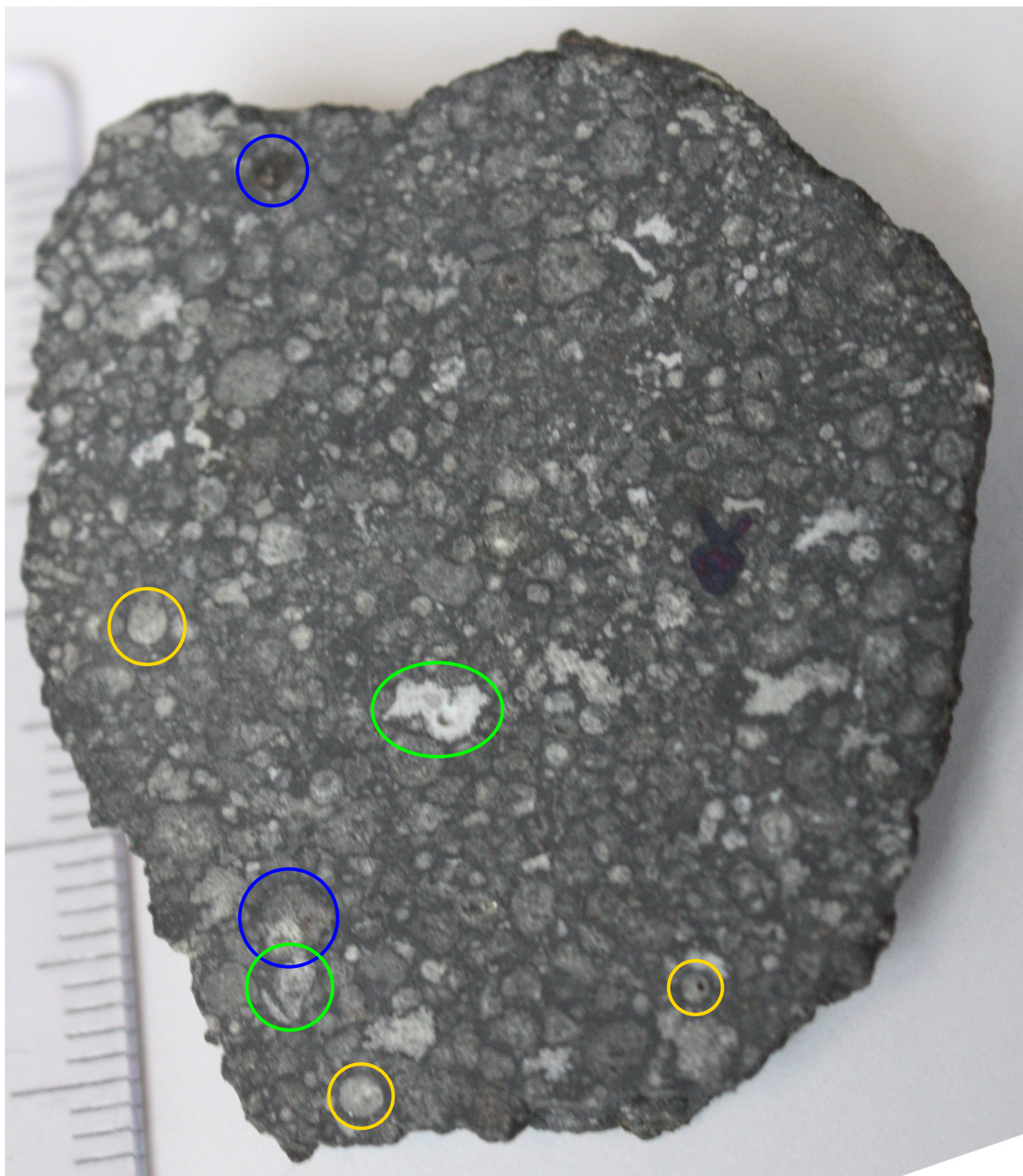


Figure 39: *The surface of the stone as seen in natural light. Enlarged picture of figure 25.*

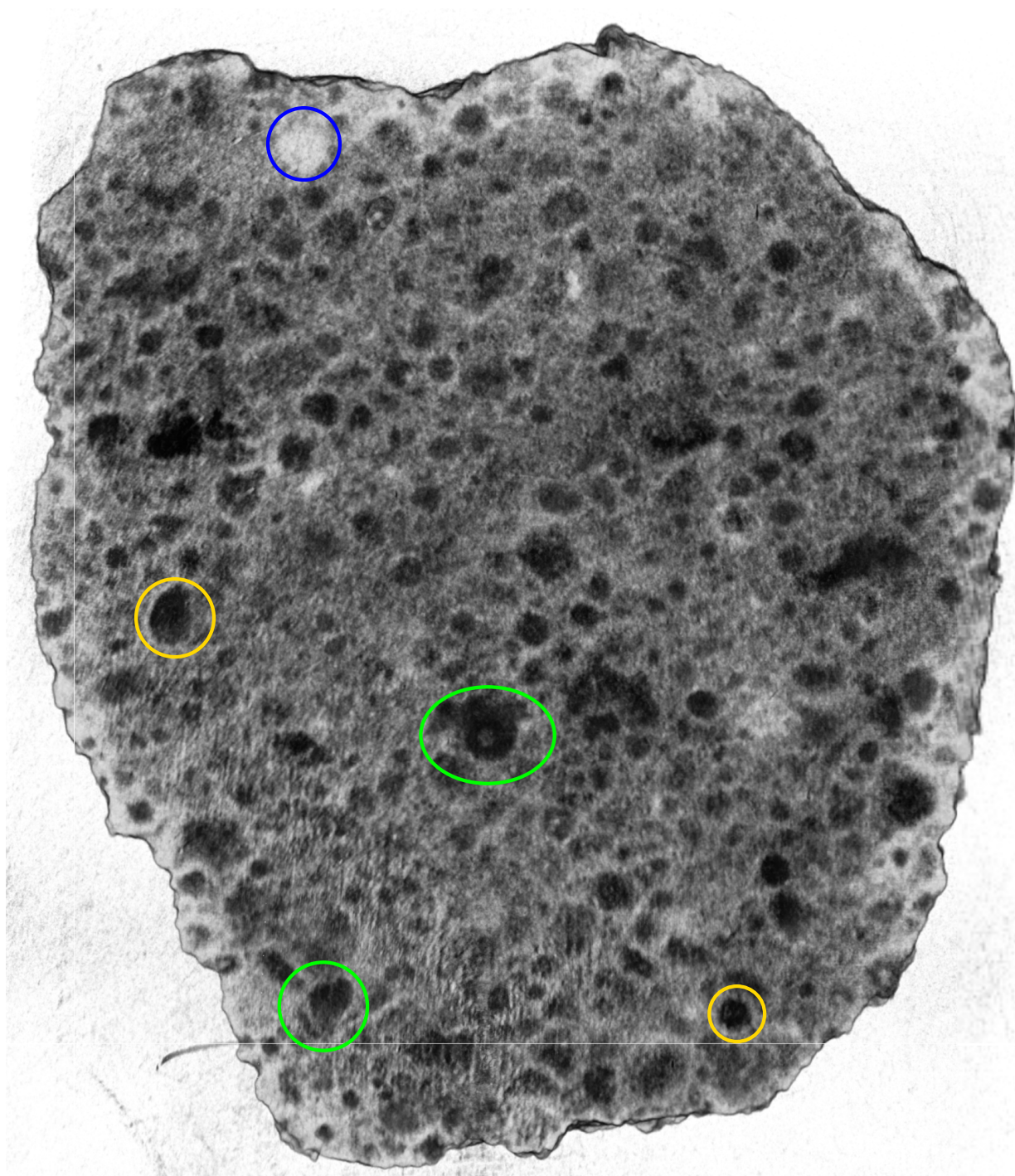


Figure 40: *The surface of the stone as seen by neutrons. Enlarged picture of figure 25.*